

AD-A239 226



REPORT DOCUMENTATION PAGE			Form Approved OMB No. 2704-0188	
<small>Public reporting burden for this report is estimated to be 1 hour per response, including the time for reviewing instructions, searching existing data sources, gathering and maintaining the data needed, completing and reviewing the collection of information, and reviewing and approving the collection of information. Send comments regarding this burden estimate or any other aspect of this collection of information, including suggestions for reducing this burden, to Washington Headquarters Service, Directorate for Information Operations and Reports, 1215 Jefferson Davis Highway, Suite 1204, Arlington, VA 22202-4302, and to the Office of Management and Budget, Paperwork Project Director, 1215 Jefferson Davis Highway, Suite 1204, Arlington, VA 22202-4302.</small>				
1. AGENCY USE ONLY (Leave blank)	2. REPORT DATE	3. REPORT TYPE AND DATES COVERED THESIS/DOSSERTATION		
4. TITLE AND SUBTITLE Development of a High-Resolution Low Energy Electron Diffraction System		5. FUNDING NUMBERS		
6. AUTHOR(S) Brian L. Clothier, Captain				
7. PERFORMING ORGANIZATION NAME(S) AND ADDRESS(ES) AFIT Student Attending: University of Texas		8. PERFORMING ORGANIZATION REPORT NUMBER AFIT/CI/CIA- 91-052		
9. SPONSORING/MONITORING AGENCY NAME(S) AND ADDRESS(ES) AFIT/CI Wright-Patterson AFB OH 45433-6583		10. SPONSORING/MONITORING AGENCY REPORT NUMBER		
11. SUPPLEMENTARY NOTES				
12a. DISTRIBUTION/AVAILABILITY STATEMENT Approved for Public Release IAW 190-1 Distributed Unlimited ERNEST A. HAYGOOD, 1st Lt, USAF Executive Officer		12b. DISTRIBUTION CODE		
13. ABSTRACT (Maximum 200 words)				
<p>DTIC ELECTE S D AUG 08 1991</p>				
14. SUBJECT TERMS		15. NUMBER OF PAGES 84		
		16. PRICE CODE		
17. SECURITY CLASSIFICATION OF REPORT	18. SECURITY CLASSIFICATION OF THIS PAGE	19. SECURITY CLASSIFICATION OF ABSTRACT	20. LIMITATION OF ABSTRACT	

ABSTRACT

DEVELOPMENT OF A HIGH-RESOLUTION LOW ENERGY ELECTRON DIFFRACTION SYSTEM

by

BRIAN LEE CLOTHIER, B.S.

SUPERVISING PROFESSOR: JIM L. ERSKINE

➤ Spot Profile Analysis is an efficient process used to evaluate both qualitatively and quantitatively the defect structure of crystal surfaces. The process consists of analyzing the angular distribution of a Low Energy Electron Diffraction (LEED) spot. This paper describes the design, construction, and testing of a new LEED detection system which uses a position sensitive detector. The electron optics built for this system incorporate several unique design features. These features include unipotential lenses, and the use of an easily removable electron source. Preliminary testing of the system shows transfer widths in the 300 angstrom range for electron energies from 80 to 250 eV. ➤

91 8 07 143

91-07264



**DEVELOPMENT OF A HIGH-RESOLUTION LOW ENERGY
ELECTRON DIFFRACTION SYSTEM**

by

BRIAN LEE CLOTHIER, B.S.

Capt, USAF

1991

90 pages

Master of Arts awarded

by the

University of Texas at Austin

Accession For	
NTIS CRASL	<input checked="" type="checkbox"/>
DTIC TAB	<input type="checkbox"/>
Unannounced	<input type="checkbox"/>
Justification	
By	
Distribution/	
Availability Codes	
Dist	Avail. &/or Special
A-1	



Dedication

*to my wife
for her patience, love, and understanding*

Acknowledgements

The list of individuals who deserve recognition and gratitude for this thesis are too numerous to mention; however, there are several individuals that I would like to recognize. First and foremost, I would like to thank my supervising professor, Dr. Jim Erskine, for his guidance and trust. His belief in my ability to complete this project on time kept me going when things looked dismal. I would also like to thank my fellow graduate students in "Erskine's lab": in particular, Joan Yater for taking time almost every day to find something for me; Walker Hale for his vast knowledge and seemingly endless patience; and Jim Men for working day and night to help me finish this project. I am also indebted to Bill Killgore for his friendship and outstanding skill as a craftsman. His friendly advice and patience made the entire design a reality. I would like to further thank Jess Reich. He is a wonderful friend, teacher, and craftsman who taught me more than just how to be a good machinist. I am grateful to Mary Ghaleb for her kindness and cheer whenever I needed her help. She is the glue that holds Erskine's group together. Finally, I would like to thank my dear wife and closest friend, Cathy, for standing by me when I was so absorbed in my work. Her attention to the larger issues of our life made completion of this project possible.

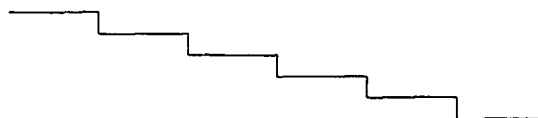
Table of Contents

I. Introduction	1
II. Electron Optics	11
Design Considerations	11
Design	16
Assembly	24
III. Power Control Unit	38
Design Requirements	38
Design	40
Testing	47
Operation	48
IV. Experimental Method	56
Experimental Apparatus	58
Experimental Procedure	64
Experimental Results	72
V. Conclusions	80
Recommendations	81
Bibliography	83

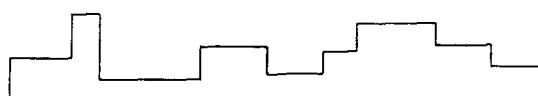
I. Introduction

Surface defects at the atomic level have been shown to affect various properties of materials. The most common surface defects are depicted (in one dimension) in Figure 1 (4, 12). The examples of these defects' effects are numerous. For instance, random step arrangements on the surface of W(110) have been shown to decrease the work function up to 0.6 eV as compared to a well annealed flat surface. Hydrogen and oxygen gas are not adsorbed onto flat surfaces of platinum whereas they are on stepped platinum. Furthermore, the surface photo-voltage from clean cleaved silicon (111) depends monotonically on the step density (4, 16). These few effects, and many others, have led to the need to characterize the long range order of the surface of materials so as to study surface defects.

The analysis of the angular distribution of the intensity of a Low Energy Electron Diffraction (LEED) spot, a process commonly called Spot Profile Analysis (SPA-LEED), is an efficient way to evaluate qualitatively and quantitatively the defect structure of crystal surfaces. Just by visually inspecting the shape of LEED spots, one can gain *qualitative* information about atomic steps and island growth on crystal surfaces. Some examples of this obtainable *qualitative* information are summarized in Table 1 (3, 181). Splitting of a spot indicates regular atomic steps, while broadening of the spot indicates random steps. A ring structure about a spot is indicative of many atomic islands of identical size or many atomic islands separated by a regular distance. A ring structure that has been broadened like that of spot shape "e" in Table 1 is caused



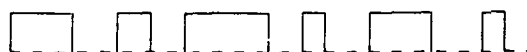
Regular steps (e.g. cleaved Si (111))



Random steps (e.g. after ion bombardment
and annealing)



Regular size islands (fraction of monolayer)



Regular distance islands
(fraction of monolayer)



Random size and distance islands
(fraction of monolayer)

Figure 1: Common Surface Defects (Cross Section of the Surface). In general, the variations in orientation of the step edges have to be considered.



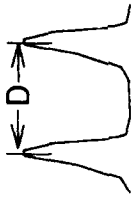
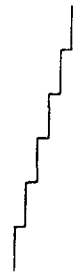


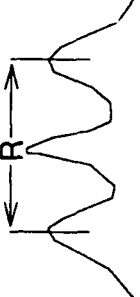
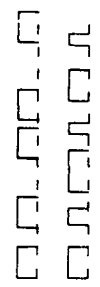
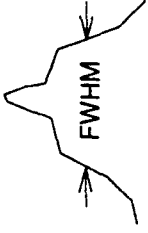
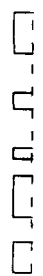
Information Extracted From LEED Spots			
Spot shape	Spot profile	Surface structure	
•			ideal surface
• •			regular steps
●			random steps
○			regular size or islands regular distance
●			random size and distance islands

Table 1: Information Deduced From Visual Inspection and Measurements of LEED Spots. The distance between islands is measured from center to center. This Table is taken from (3, 181).

by random sized islands or many islands separated by random distances. Qualitative information like this, however, is not enough.

Quantitative information is necessary to fully characterize the crystal surface. This *quantitative* information is gleaned from measured values of the full width at half maximum (FWHM), the splitting distance D , or the ring diameter R (Table 1) of the measured intensity distribution, $i(\mathbf{k})_{\text{meas}}$, of a LEED spot (3, 182). These parameters are direct measures of terrace (step) widths and island sizes or distances. The smaller the distance D , diameter R , or FWHM (Table 1), the larger are the terraces or island sizes (3, 181). Unfortunately, the limitations of the LEED experimental apparatus contribute to broadening of the LEED spots, thus limiting the size of the ordered region which can be resolved (10, 696).

Several approaches have been taken to quantify the effect the LEED instrument has on limiting the size of the ordered region which can be experimentally resolved. The following two paragraphs outline the approach given by Robert L. Park et al. (16, 61). For kinematic scattering with a given vector \mathbf{k} , the Fourier transform of $i(\mathbf{k})_{\text{true}}$ (the intensity one would measure with a perfect LEED instrument) is the *true autocorrelation function* $\Phi(\mathbf{r})$. This autocorrelation function is a measure of the number of pairs of scatterers that are connected by a real space vector \mathbf{r} . It represents the "ultimate structural information that can be derived from a diffraction measurement" (16, 61). Unfortunately, we don't measure $i(\mathbf{k})_{\text{true}}$ but $i(\mathbf{k})_{\text{meas}}$. Now $i(\mathbf{k})_{\text{meas}}$ can be expressed as the convolution product of $i(\mathbf{k})_{\text{true}}$ and the *instrument response*

function $T(\mathbf{k})$, which is the response of the LEED instrument to a diffracted beam from a hypothetical perfect, rigid crystal surface:

$$i(\mathbf{k})_{\text{meas}} = i(\mathbf{k})_{\text{true}} * T(\mathbf{k}).$$

Taking the Fourier transform of both sides and using the convolution theorem we see:

$$\begin{array}{ccccc} \text{Measured autocorrelation} & = & \text{True autocorrelation} & \times & \text{Transfer} \\ \text{function} & & & & \\ \text{function } Q(\mathbf{r}) & & \text{function } \Phi(\mathbf{r}) & & t(\mathbf{r}) \end{array}$$

where $Q(\mathbf{r})$ is the Fourier transform of $i(\mathbf{k})_{\text{meas}}$, and the *transfer function* $t(\mathbf{r})$ is the Fourier transform of $T(\mathbf{k})$.

The effect of the LEED instrument on the true autocorrelation function $\Phi(\mathbf{r})$ can be deduced from the above equation but is easier illustrated by Park's simple one dimensional example shown in Figure 2 (6, 213). This figure shows that the effect of the transfer function is to suppress long range correlations in the Measured autocorrelation function $Q(\mathbf{r})$. Thus, according to Park, "the diffraction instrument is effective as an interference detector only over a limited range given by the width of the transfer function" (6, 213). This width, hereafter called the *transfer width* $w[t(\mathbf{r})]$, is considered the instrumental limit for the detection of terrace widths and island sizes. Remembering that what is measured in a LEED experiment is $i(\mathbf{k})_{\text{meas}}$ of a spot and realizing that its FWHM (defined now as j) can only be measured to an accuracy "a" of $\Delta j/j$, one can combine this accuracy

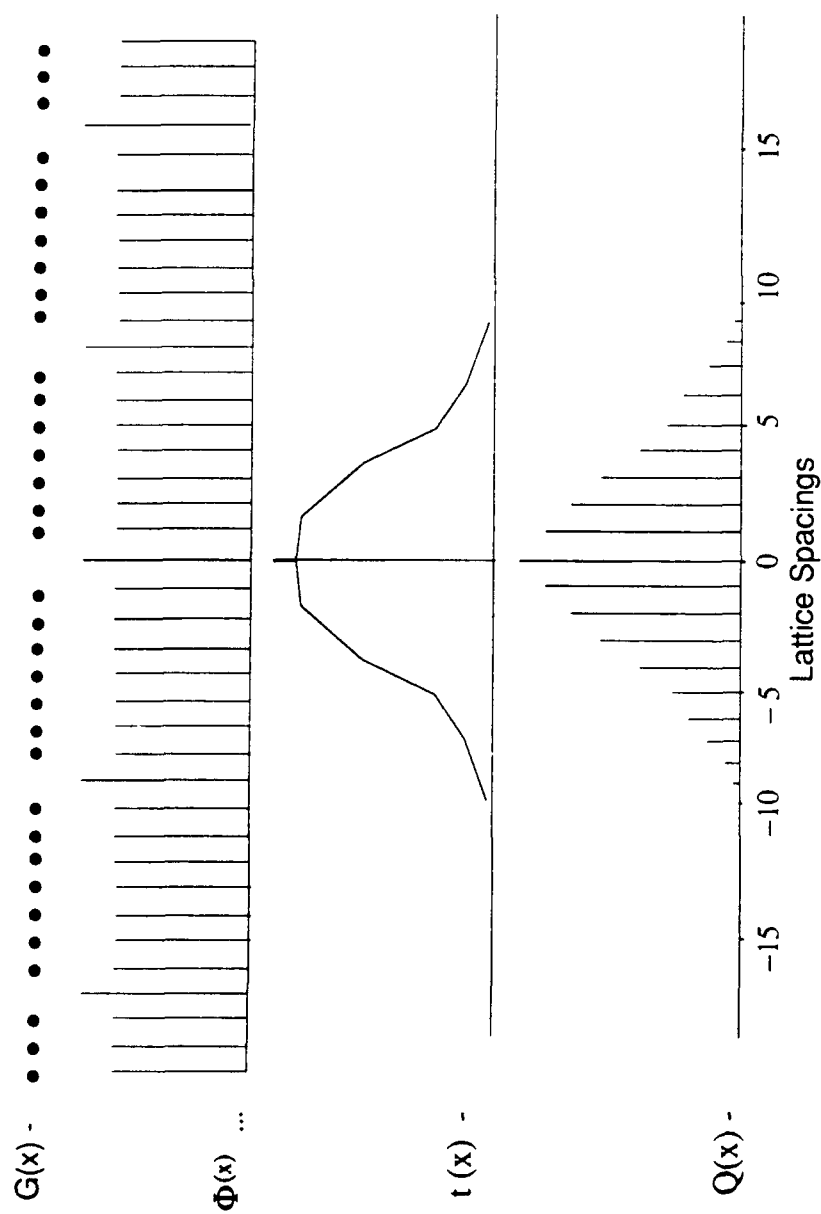


Figure 2: The Suppression of Long Range Correlations by the Transfer Function $t(x)$. $G(x)$ represents an infinite chain in which every eighth point is missing. $\Phi(x)$ is the true autocorrelation function of the chain. $t(x)$ is the hypothetical instrument transfer function. $Q(x)$ is the measured autocorrelation function. The fundamental periodicity is evident in $Q(x)$, but the superperiod (every 8th missing) is not. (6, 213)

"a" with the transfer width $w[t(r)]$ to define the *maximum resolvable distance* of the LEED apparatus "d" (3, 182):

$$d = w[t(r)] / (2a)^{1/2}.$$

In order to detect island sizes or terrace widths larger than about 10 nm, the typical maximum resolvable distance d for a commercial LEED system, either the transfer width $w[t(r)]$ or the accuracy a must be increased (3, 182) (7, 2948). The purpose of this paper is to report on our efforts to construct a LEED system whose transfer width leads to a "d" much greater than 10 nm.

Before discussing the design of our LEED system, it is important review the various factors which affect the transfer width. The following breakdown into contributing factors provides a guide to designing an improved system. First of all, the components of any LEED system include the electron optics (beam source), a sample holder, and some sort of detection system, all operated in an ultra-high vacuum (UHV) chamber. Due to these components, there are four major factors which contribute to the limited *total instrument response function* $T(k)_{total}$, and thus to a limited transfer width: the electron source extension $T_1(k)$, the incident electron beam diameter $T_2(k)$, the detector aperture diameter $T_3(k)$, and the energy spread of the beam $T_4(k)$. There are many other factors, but these are all of lesser importance (15, 76). Several of these factors $T_n(k)$ are energy and angle dependent, therefore the transfer width is in general a function of primary beam energy and diffraction geometry.

Table 2 gives a brief summary of each of the four major factors $T_n(\mathbf{k})$ and the formula required to compute its contribution to the transfer width (18, 30) (16, 62).

If we assume that $T_1(\mathbf{k})$ through $T_n(\mathbf{k})$ can be represented as Gaussian, then

$$T(\mathbf{k})_{\text{total}} = T_1(\mathbf{k}) * T_2(\mathbf{k}) * T_3(\mathbf{k}) * T_4(\mathbf{k}) * \dots T_n(\mathbf{k})$$

and the FWHM of $T(\mathbf{k})_{\text{total}} = \{ \text{sum over } n \text{ of } (\text{FWHM } [T_n(\mathbf{k})])^2 \}^{1/2}$. Now since the *transfer function* $t(\mathbf{r})$ is the Fourier transform of $T(\mathbf{k})_{\text{total}}$, then the *transfer width* $w[t(\mathbf{r})]$ is given by (18, 29):

$$w[t(\mathbf{r})] = \{ \text{FWHM } [T(\mathbf{k})_{\text{total}}] \}^{-1}.$$

It has been shown by Park et al. and Lagally et al. that the most significant contributions to a limited transfer width are the electron source extension $T_1(\mathbf{k})$, and the incident electron beam diameter $T_2(\mathbf{k})$, both contributing to a broadened beam at the detector (16, 64), (9, 1276). With this in mind, our goal is to construct an electron beam source (which will hereafter be called *the electron optics*) which would limit the size of the diffracted beam, thus leading to an improvement in transfer width over its commercial counterparts. The remainder of this paper describes the design, construction, operation, and testing of a new electron optics system, including the required power control unit, and reports the

The following summary is based on the diffraction geometry shown here:
 The azimuthal angle is assumed the same. Conservation of momentum of the electron parallel to the surface gives:

$$S_{\parallel} \equiv k_{\text{parallel out}} - k_{\text{parallel in}} = \left[\frac{(2mE)^{1/2}}{h/2\pi} \right] (\sin \theta - \sin \theta_0)$$

where S_{\parallel} is the magnitude of the momentum transfer in a direction parallel to the crystal surface.

Contributor	T1(k): Electron source extension	T2(k): Incident electron beam diameter	T3(k): Detector aperture diameter	T4(k): Beam energy spread
Reason for Contribution	For a finite source size, there is an uncertainty in the angle of incidence of the beam at the crystal equal to the angle (defined as γ) subtended by the source as viewed from the crystal through the lens of the electron optics. A point source gives no uncertainty.	$\Delta\theta$ shown below gives rise to uncertainty in S_{\parallel} shown below:	$\Delta\theta$ shown below gives rise to uncertainty in S_{\parallel} shown below:	A spread in the beam energy is also a spread in the momentum of the beam we detect.
Formula for FWHM $T_n(k)$	take the partial of S_{\parallel} w.r.t. θ_0 , then FWHM $T1(k) = \left[\frac{(2mE)^{1/2}}{h/2\pi} \right] \gamma \cos \theta_0$	FWHM $T2(k) = \left[\frac{(2mE)^{1/2}}{h/2\pi} \right] \left[\frac{D}{R} \right] \frac{\cos^2 \theta}{\cos \theta_0}$ D = beam diameter R = distance from crystal to detector	FWHM $T3(k) = \frac{2\pi}{h} (2mE)^{1/2} \left[\frac{d}{R} \right] \cos \theta$ d = geometrical diameter of aperture R = distance from crystal to detector	take the partial of S_{\parallel} w.r.t. E , then FWHM $T4(k) = \frac{2\pi [m]^{1/2}}{h [2E]} \Delta E (\sin \theta - \sin \theta_0)$

Table 2: Summary of Contributions to the Transfer Width of a LEED System.

progress made in determining the transfer width of a SPA-LEED system using these optics with a commercially available position sensitive detector.

II. Electron Optics

This chapter will concentrate on describing the design considerations, design, and assembly of the electron optics built for this SPA-LEED system. A section on assembly is included in case the electron optics need repair or re-assembly. For discussion purposes, the electron optics will be broken down into three major components: the triode *electron gun*, composed of a LaB₆ cathode and two aperture lenses, the *lens column*, consisting of two identical einzel lenses and a steering lens, and the *gun housing*.

Design Considerations

In choosing a design we had several considerations. Of course, the first and foremost consideration was to maximize the transfer width, and thus the maximum resolvable distance, d , of the LEED system. However, we also wanted to build electron optics which would be easy to construct *and* operate. Furthermore, we wanted electron optics which could be altered later, so as to test various configurations of electron sources, apertures, and lens designs all in the *same gun housing*.

With these considerations in mind, the first choice became the type of electron source to employ. The two principle types of electron sources to choose from are thermionic sources, such as tungsten or LaB₆ cathodes, and field emission sources. Field emission sources have several advantages. First, they are intrinsically brighter (brightness defined as the emission current per unit solid angle) than thermionic sources (7, 2946)(2, 2642). However, as Yijian Cao and Edward H. Conrad report in their article "High q-resolution electron gun for low

energy electron diffraction", at "the low energies used in most LEED experiments (typically <500 eV), the space-charge force in the beam limits the usable current, and the brightness advantage of field emission sources is lost (at least when compared to LaB₆ cathodes)" (2, 2643). Also, our intent to use a pulse-counting position sensitive detector with a gain of 5×10^7 further reduces the brightness advantage of the field emission source (13, 8).

The second advantage of field emission sources is that they contribute less thermal energy spread (one of the four main contributors to a decreased transfer width) to the beam, than do thermionic sources. However, as was pointed out earlier, it has been found that ΔE is not the most important contributor to increased transfer width (16, 64)(9, 1276). In fact, for low order diffracted beams which provide the best resolution for studies of surface defects, the effect of electron energy spread on transfer width is small (15, 4). Typical values of ΔE for field emission sources are reported in the literature as varying from 0.15 - 0.25 eV at room temperature (7, 2946). Thermionic sources contribute ΔE 's varying typically between 0.2 and 0.6 eV, depending upon the filament temperature, with LaB₆ cathodes performing better than their tungsten counterparts (11, 1)(7, 2945).

Despite these slight advantages for field emission sources, we chose to use a LaB₆ thermionic source because for *three* reasons it allows electron optics which are easier to operate. *First*, use of the LaB₆ cathode allows control of beam current without affecting the focus of the beam. To increase the beam current, only the temperature of the LaB₆ filament must be increased. This may

be done by simply passing more current through a directly heated filament via a power source different from that used to control lens voltages. This independent control of beam current is not possible with field emission sources. For field emission sources, the beam current is a function of the field produced by the cathode-anode potential (2, 2642). Therefore, a beam current adjustment requires adjustment of the cathode-anode potential, resulting in beam defocusing.

Second, to maintain a stable current with a field emission source, careful cleaning of the tip and anode must be done *after every bake out*. Park et al. report radiative heating at 350° C for up to 24h followed by successive flashing of the tip as requirements (7, 2947). Comparatively, life with a LaB₆ cathode is easy, requiring just 15-20 minutes of running at reduce filament current to remove oxides (11)

Third, and most important, use of a thermionic source allows one to take advantage of the focal length scaling properties of the triode electron gun system and einzel lenses. A simple triode electron gun employing a point cathode is shown in Figure 3 (8, 372). The focal properties of such a system are solely a function of the geometrical distances c , a , r_g and r_a and the ratios of $V_{grid}/V_{cathode}$, and $V_{aperture}/V_{cathode}$ (8, 345). An 'einzel' (literally meaning single) lens is a multielectrode lens to which only one voltage is applied. One of the most common types, the three-diaphragm einzel lens, is shown in Figure 4 (8, 84). The focal length of this type of lens depends upon the aperture radii R_o and R_i , the spacings S , the thicknesses T_o and T_i of the diaphragms, and scales as the

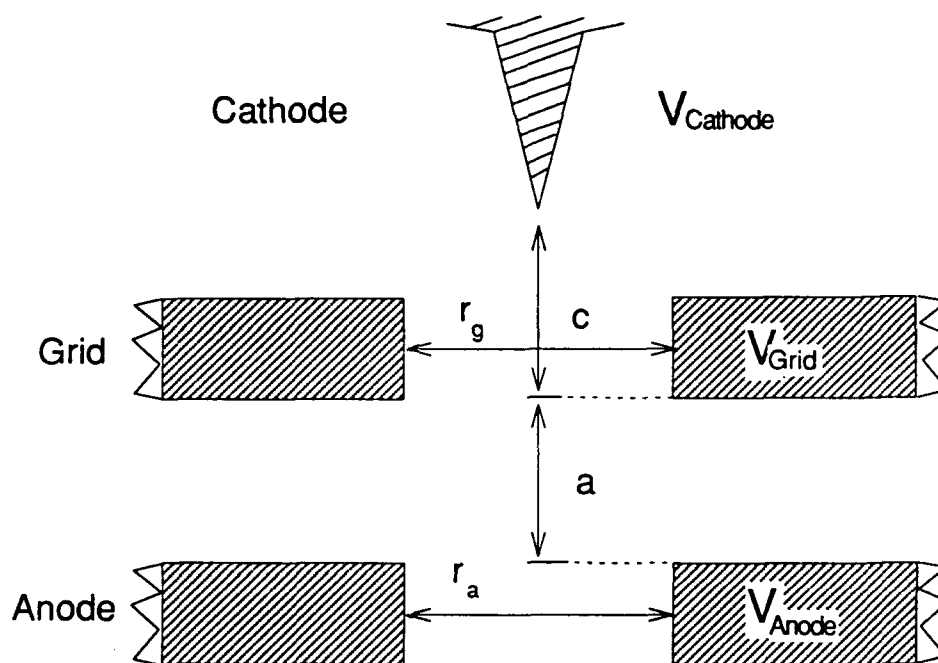


Figure 3. Triode Electron Gun. This schematic shows the critical geometric distances c , a , $r(\text{grid})$ and $r(\text{aperture})$ which are factors in the focal length of this system. Note that c and a are the distances of the cathode and anode, respectively, from the top surface of the grid electrode.

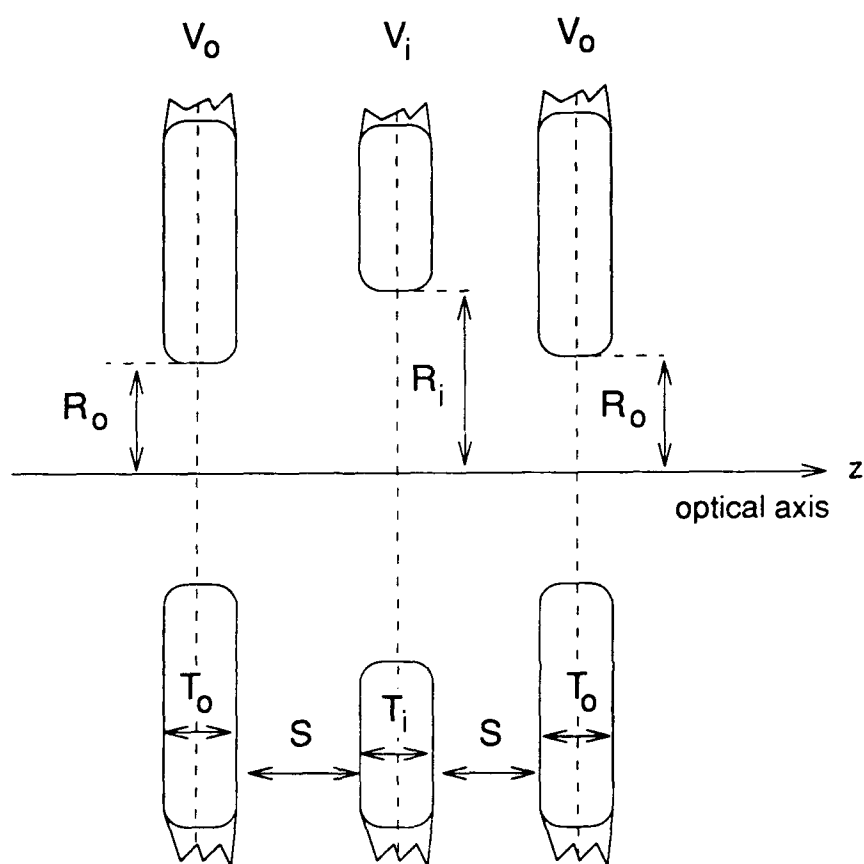


Figure 4. Three-Diaphragm Einzel Lens. This cross-section shows the important geometric parameters which affect the focal length.

ratio V_i/V_e (where V_e is the voltage at which the electron beam would have zero velocity, i.e., V_{cathode}) (2, 2642) (8, 83). By using the focal length scaling properties of these two systems, it is in principle possible to use just one power supply to bias both the cathode and all lenses. Furthermore, once the optimum focal ratios of $V_{\text{lens}}/V_{\text{cathode}}$ are adjusted by potentiometer, changing the beam energy by changing V_{cathode} should not defocus the beam. This convenience would *not* be available for field emission sources. Here the cathode-anode bias is kept constant to ensure a constant beam current. To adjust the beam energy an accelerator stage's voltage must be changed, resulting in defocusing of the beam (2, 2642)

Design

With the above design considerations in mind, we chose to modify an existing design which already exploited the stated advantages of the LaB₆ cathode. The electron optics built for our SPA-LEED system are a derivative of a design by Yijian Cao and Edward H. Conrad (2, 2642). Figure 5 is a reprint of this design proposed in their article "High q-resolution electron gun for low energy electron diffraction." Our electron optics maintain all the critical lens dimensions noted in Figures 3 and 4 plus the distances L1, L2, and L3 reprinted in Figure 5. We also designed our system's accompanying electronics to achieve the range of ratios $V_{\text{lens}}/V_{\text{cathode}}$ published in their paper (more on this in **Section III**). Furthermore, we hope to come close to achieving the performance of their optics system. Cao and Conrad report beam currents as high as 25 nA

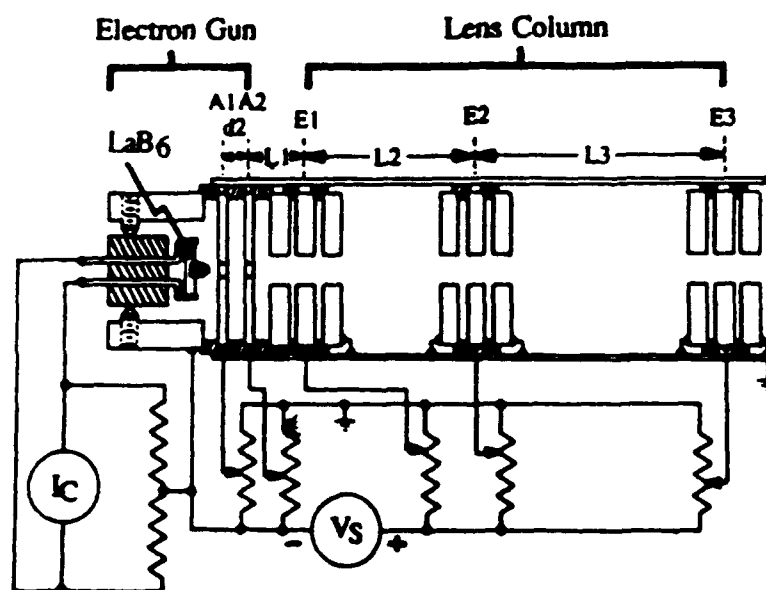


FIG. 1. Schematic drawing of the electron gun and lens column. The indirectly heated LaB₆ cathode is mounted on the cathode base and positioned on the optical axis, using three adjustment screws. The cathode to anode A1 distance is 1.23 mm. The spacing between the remaining lens elements, d2, L1, L2, and L3 are 1.94, 7.15, 32.4, and 57.6 mm, respectively. The electron energy is controlled by adjusting the supply voltage V_S . The cathode temperature is set by the current supply I_C , floating at the cathode potential V_C .

Figure 5. Reprint of Cao and Conrad's Electron Optics Design.

and a beam spot size between 50 and 114 μm for energies between 500 and 100 eV, respectively, at a gun-to-detector working distance of 6.69 in. (2, 2642).

Their reported measurements of the transfer width of a LEED system employing this optics design are reprinted in Figure 6.

Our modified electron optics are shown schematically in Figure 7. Our modifications fall into three main areas: the incorporation of a self-contained electron gun which can be easily removed for cathode replacement or future modifications, the addition of a steering lens at E2, and the method of construction which we feel is straightforward and makes future testing of new sources and lens systems possible *within the same gun housing*. Each of these modifications will be addressed in the following discussion of the electron optics.

The electron optics basically consist of a *triode electron gun*, a *lens column* of two identical einzel lenses E1 and E3 and a steering lens E2, and a single grounded *gun housing* which shields them all. All critical dimensions have been machined to tolerances of plus or minus .001". Sapphire balls and rods have been used where insulated spacing is required.

The triode electron gun is shown in Figure 8. It consists of a grid A1 and anode A2 whose thicknesses and aperture diameters are .020". The critical distances, c and a (see Figure 3), are .048" and .046" respectively. The electron source is a directly heated single crystal LaB₆ cathode whose conical tip has been ground to produce a 10 μm flat. The cathode has been aligned within .002" of the optical axis of A1 and A2 by adjustment of three positioning set screws. According to Cao and Conrad, at $V_{A1}/V_{\text{cathode}} = 0.98$ and $V_{A2}/V_{\text{cathode}} =$

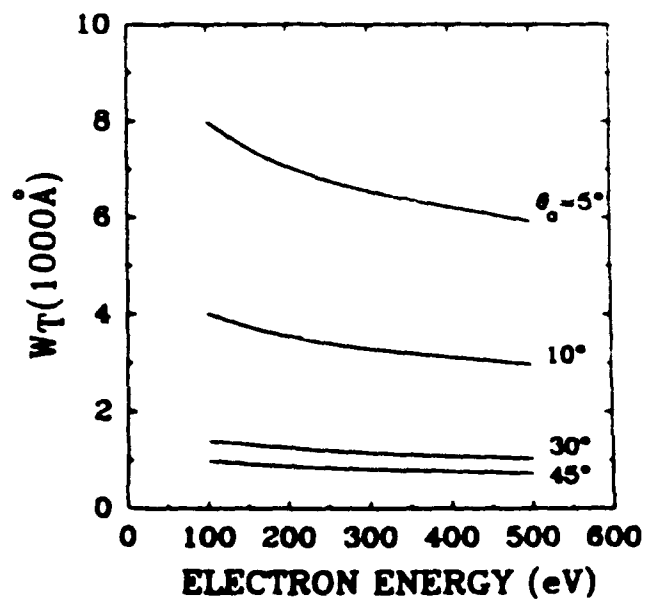


FIG. 5. The transfer width of the system [calculated from Eq. (1) and the experimental data of Fig. 4] as a function of electron energy for the specular diffraction beam.

Figure 6. Reported Performance of Cao and Conrad's Electron Optics Design.

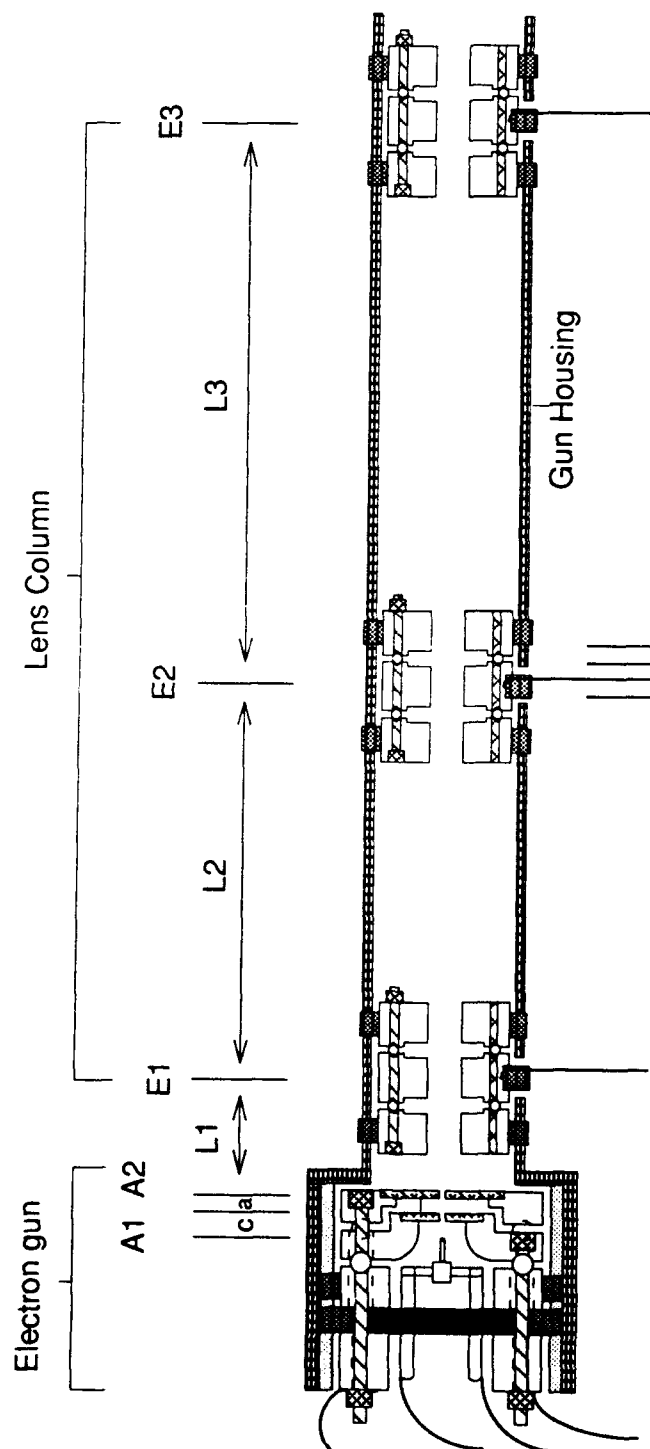


Figure 7. Schematic Drawing of the Electron Optics. The LaB_6 cathode is positioned on the optical axis by three adjustment screws, prior to sliding the entire electron gun into the gun housing. The cathode to grid A1 distance c is .048 in. The distance a is .046 in.. The distances $L1$, $L2$, and $L3$ between the centers of remaining lens elements are .281, 1.276, and 2.268 inches, respectively. All electrical leads are connected to the power control unit. E2 has four leads due to it being a steering lens.

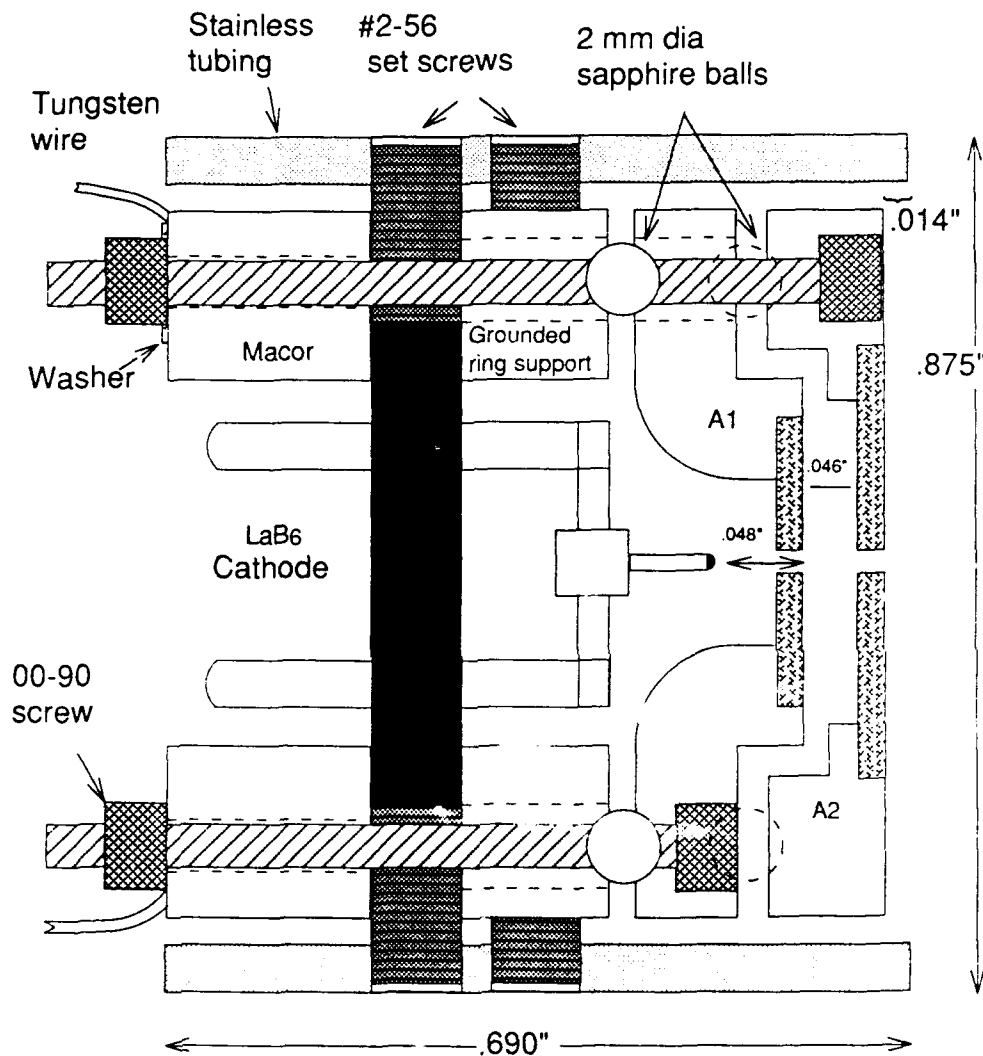


Figure 8. Cross Section of Self-contained Electron Gun. This entire unit slides snugly into the gun housing after the cathode has been aligned on the optical axis of A1 and A2 via an optical microscope.

0.44, this triode system should produce a virtual image of the cathode approximately 13 cm to the left of E1 (2, 2642).

The electron gun is 'self-contained', meaning that it is assembled separately from the gun housing, and slides into the gun housing. It is secured there with a set screw. This has several advantages. It allows easier alignment of the cathode with A1 and A2 because the microscope need only peer through A2 to the cathode instead of through the entire lens column first. Furthermore, this electron gun design allows the entire electron gun to be slid out of the gun housing to replace a cathode without removing the entire optics system from its chamber mount. Finally, this arrangement allows other electron sources to be easily substituted into the gun housing for future tests using the same lens column. A possible problem of misalignment of the optical axis of the electron gun with that of the lens column is overcome by the assembly method described later.

The lens column is composed of two identical einzel lenses E1 and E3, and a steering lens E2. These lenses are mounted on the optical axis defined by A1 and A2 to within 11 mrad, .8 mrad, and .2 mrad respectively (see **Assembly** section for details). A schematic of E1 and E3 is shown in Figure 9. This Figure shows that the critical distances R_O and R_i are the same at .075", S equals .050", while T_O and T_i are identical at .135". These distances are identical to those used by Cao and Conrad (2, 2643). Studies have shown that three diaphragm einzel lenses with equal aperture radii R_O and R_i suffer much lower spherical aberration than do those of unequal radii (8, 185). V_O , the potential of the two outside diaphragms, is maintained at ground. V_i is biased positively with respect to

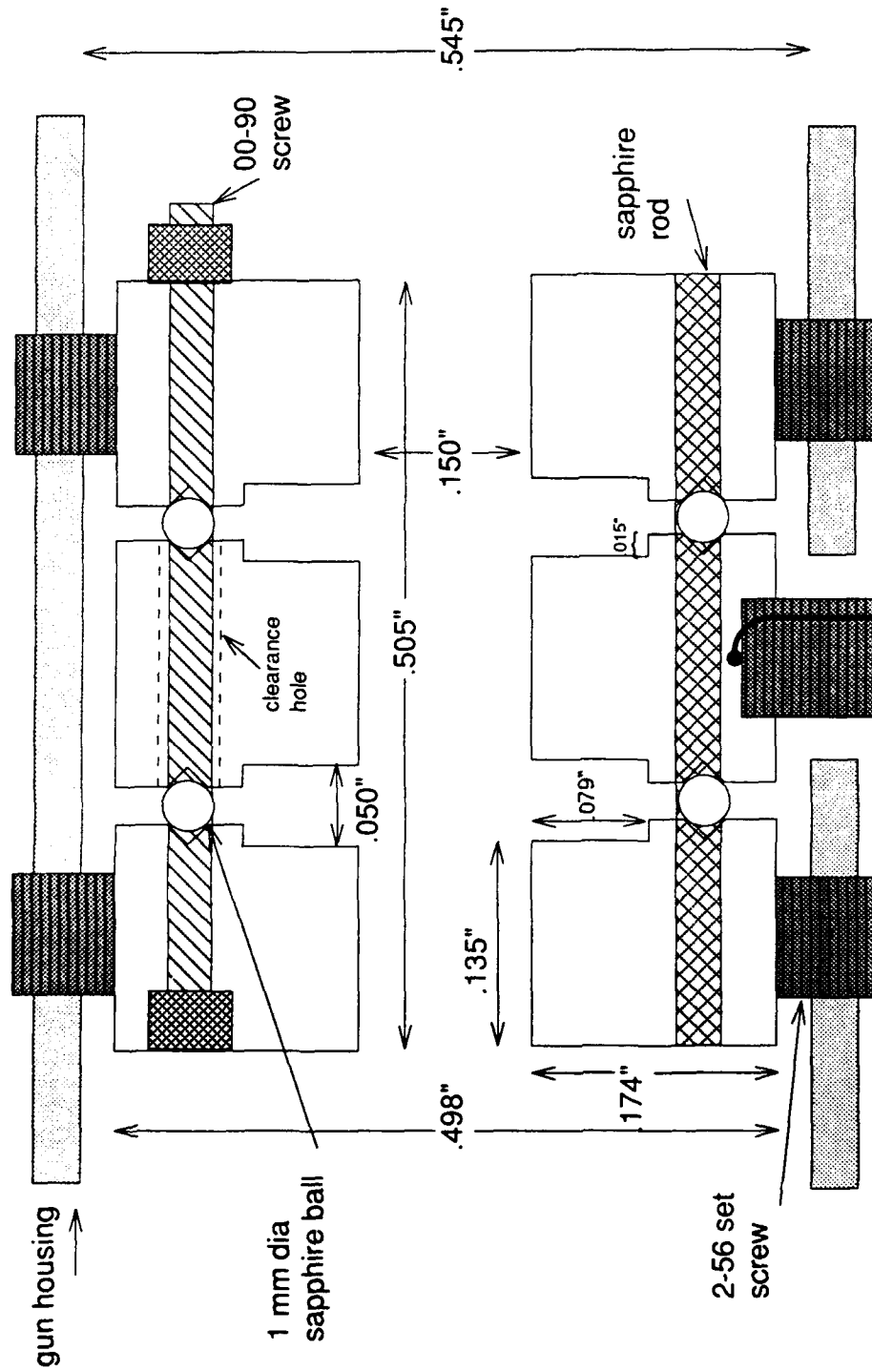


Figure 9. Cross Section of E1 and E3.

ground, thus initially accelerating the electron beam and causing it to travel much nearer the optical axis than would occur with a negatively biased V_1 (8, 83). This effect is employed to reduce aberrations by providing a more nearly paraxial beam.

Another means employed to reduce aberrations is the steering lens E2. By electrostatically deflecting the beam within the lens column, it is possible to compensate for misalignment errors inherent in attempting to place E1, E2, and E3 on the same optical axis. The design for our steering lens is shown in Figure 10. Disregarding for a moment the center diaphragm's four .020" gaps which create four symmetric pieces instead of one cylinder, this lens has the same critical geometric measurements as E1 and E3. Also similar is the ability to bias the center diaphragm, as a whole, positively with respect to the grounded outer diaphragms. The differences are the narrow gaps and that opposite pole pieces of the center diaphragm may be differentially biased at up to 10% of the base potential (call it V_{ave}) of the whole center diaphragm. Although we have done no field plotting or ray tracing for this arrangement, it is assumed that this lens will behave as an einzel lens with the ability to deflect the incident beam. Preliminary experimental observations will be reported later in this paper.

Assembly

Assembling the electron optics is a tedious task made easy by the use of the assembly tools shown in Figures 11 and 12 and by following the instructions in this section. All references to individual metal pieces will use the names (in

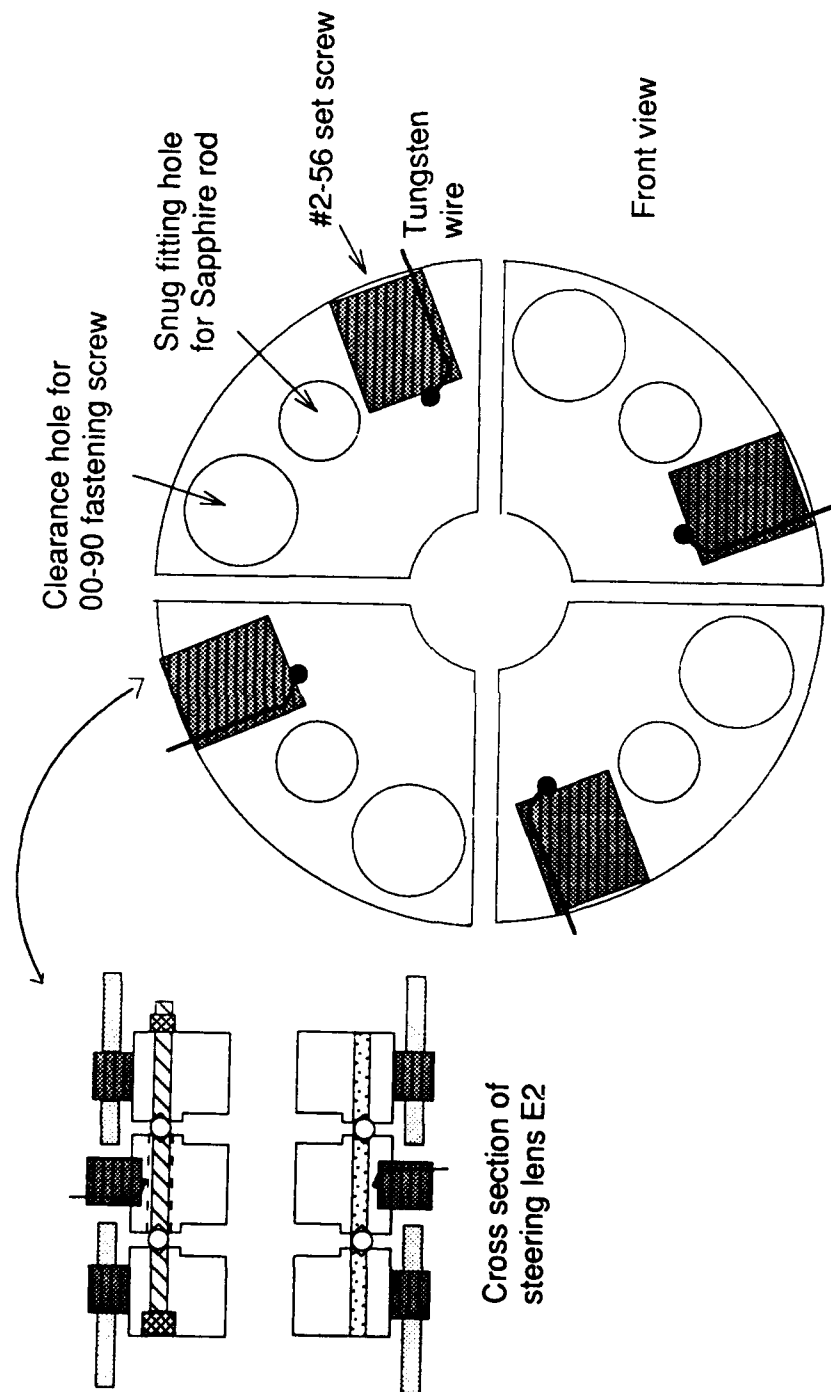


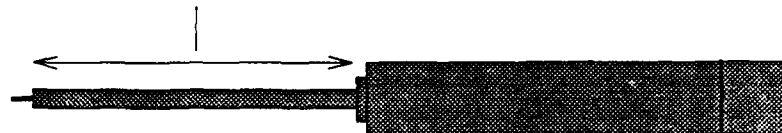
Figure 10. Cross Section of Steering Lens E2. Front view blowup of center cylinder shows the four biased steering lens pieces.

This distance is machined precisely to provide the distance L_1 between A2 and E1



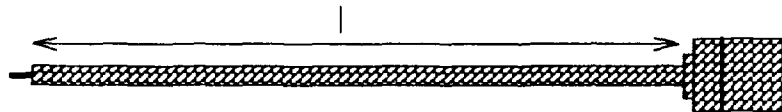
Assembly Tool #1

This distance is machined precisely to provide the distance L_2 between A2 and E2



Assembly Tool #2

This distance is machined precisely to provide the distance L_1 between A2 and E3



Assembly Tool #3



Assembly Ring

Figure 11. Assembly Tools. These tools are needed to place E1, E2, and E3 in their proper positions on the optical axis.

This .020" dia shaft fits snugly into both apertures A1 and A2, thus ensuring their alignment. Its height is set so as not to touch the cathode during assembly.

This ledge provides the proper distance between A2 and the front edge of the electron gun tubing, thus ensuring the proper distance between A2 and E1.

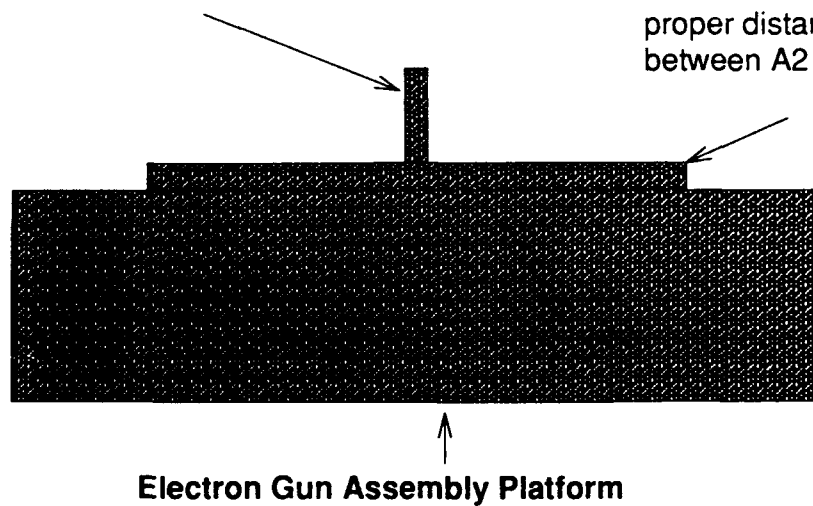


Figure 12: Cross Section of the Electron Gun Assembly Platform Necessary to Construct the Electron Gun.

capital letters) given them in the machine shop drawings. To be systematic, this section will describe the assembly procedure in stages. This assembly procedure allows the entire electron optics system to be assembled by one person in one day.

Stage I: Electron Gun Assembly

Refer to Figure 13 during this discussion. Place the Electron Gun Assembly Platform on a clean, flat surface. Place four Fastening Screws into the four countersunk holes of the Second Aperture Holder portion of A2 so that the screw heads are firmly in the countersinks. Carefully insert the aperture hole of A2 over the shaft on the Assembly Platform until A2 seats flatly against the ledge. All four Fastening Screws should be pointing away from the Assembly Platform at this time and the groove in A2 should be visible. Place the two .060" diameter sapphire rods in their holes in A2. They should be pointed parallel to the Fastening Screws and seated firmly against the ledge. Fill the groove with .020mm diameter sapphire balls.

Take the First Aperture Holder portion of A1 and place four Fastening Screws into it just as was done for A2. By holding these screws, lower A1 over A2, carefully inserting all of A2's screws through the clearance holes in A1 and the sapphire rod through its appropriate holes. The aperture hole of A1 should fit over the shaft of the Assembly Platform. There should now be eight screws and two sapphire rods pointing upward from the Assembly Platform. The sapphire balls should fit snugly between the grooves of A1 and A2. Now fill A1's groove with .020mm diameter sapphire balls.

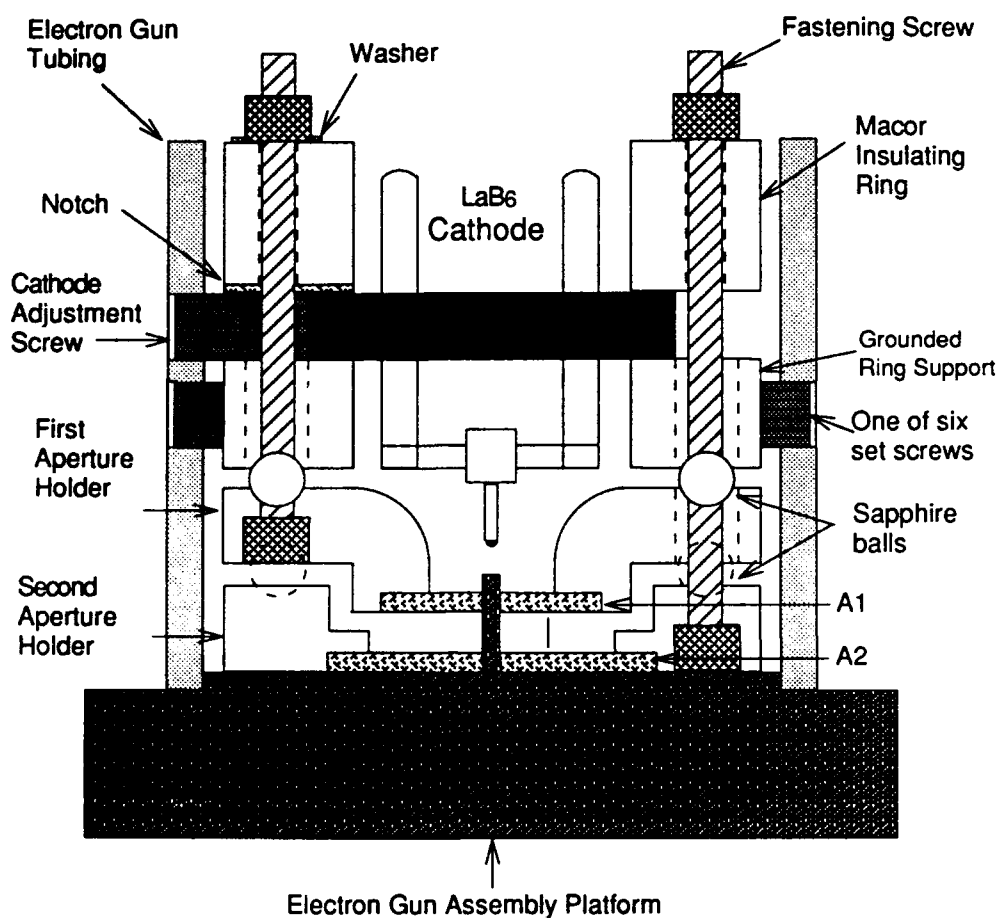


Figure 13: Assembly Method for the Electron Gun. The Electron Gun must be assembled on this platform so as to maintain proper distance between A2 and E1. A washer has been placed on one of the electrodes (Fastening Screws) of A1 to differentiate it from A2.

Place the Grounded Ring Support, groove pointed downward, over the eight screws and two sapphire rods pointing upward from A1. The sapphire balls should fit snugly between the grooves of A1 and the Grounded Ring Support. Now carefully place the LaB₆ cathode assembly, cathode pointing toward the Assembly Platform, on the Grounded Ring Support so that the black ceramic cathode base is somewhat centered between all the screws.

Take the Macor Insulating Ring and place it (notches toward cathode base) over the eight screws rising out of A1. The sapphire rod has been cut so that it does not extend into the Macor Ring. The Macor Ring should fit snugly over the ceramic base of the LaB₆ cathode. Now secure the entire stack by fitting the eight Fastening Screws with their nuts and tighten. Note that a washer has been placed over one of the four Fastening Screws which makes electrical contact with A1 to differentiate it from those which contact A2. Leave this "stack" on the Assembly Platform at this time.

Place the Electron Gun Tubing (six set screw holes closer to the Assembly Platform) over the "stack" until it seats firmly against the Assembly Platform. Rotate the Tubing until the three cathode adjustment screw holes are aligned with the notches in the Macor Ring. Insert three #2-56 by 3/16" stainless set screws into the cathode adjustment screw holes and screw in until they touch the black ceramic cathode base. These screws will be used to align the cathode with the two aperture holes later. Now insert six #2-56 by 1/16" stainless set screws into their holes in the Tubing. These screws are used to grab the Grounded Ring Support to secure the "stack" to the Electron Gun Tubing. They must be tightened evenly

to leave equidistant clearance between the Macor Insulating Ring and the Electron Gun Tubing. Care must be taken to ensure the Tubing still seats snugly against the Platform after securing is complete. Furthermore, once securing is complete, none of the six set screws should protrude beyond the outside wall of the Tubing. Assembly of the Electron Gun is now complete except for alignment of the LaB₆ cathode on the optical axis. Remove the entire electron gun from the Assembly Platform now by gently lifting straight up.

Stage II: Cathode Alignment on the Optical Axis

The alignment of the LaB₆ cathode is done using an optical microscope. High intensity light is directed into the two remaining holes in the Electron Gun Tubing to illuminate the inner cavity of the Electron Gun. The microscope is used to peer through E2 and then E1 at the LaB₆ cathode, which is now clearly visible. The three cathode alignment set screws are then adjusted to bring the cathode tip to the center of the .020" aperture holes. Using this technique, we were able to center the center of the cathode flat to within .002" of the optical axis. After adjustment of the cathode, no set screws should protrude outside the walls of the Electron Gun Tubing.

Stage III: Assembly of E1 and E3

Assembly of E1 and E3, identical einzel lenses, follows a procedure similar to that used to assemble the Electron Gun. Refer to Figure 14 during the following instructions. Begin by placing Assembly Tool #1 (Figure 10) in a vice so that the pointed end points vertically upward. The lenses are both constructed

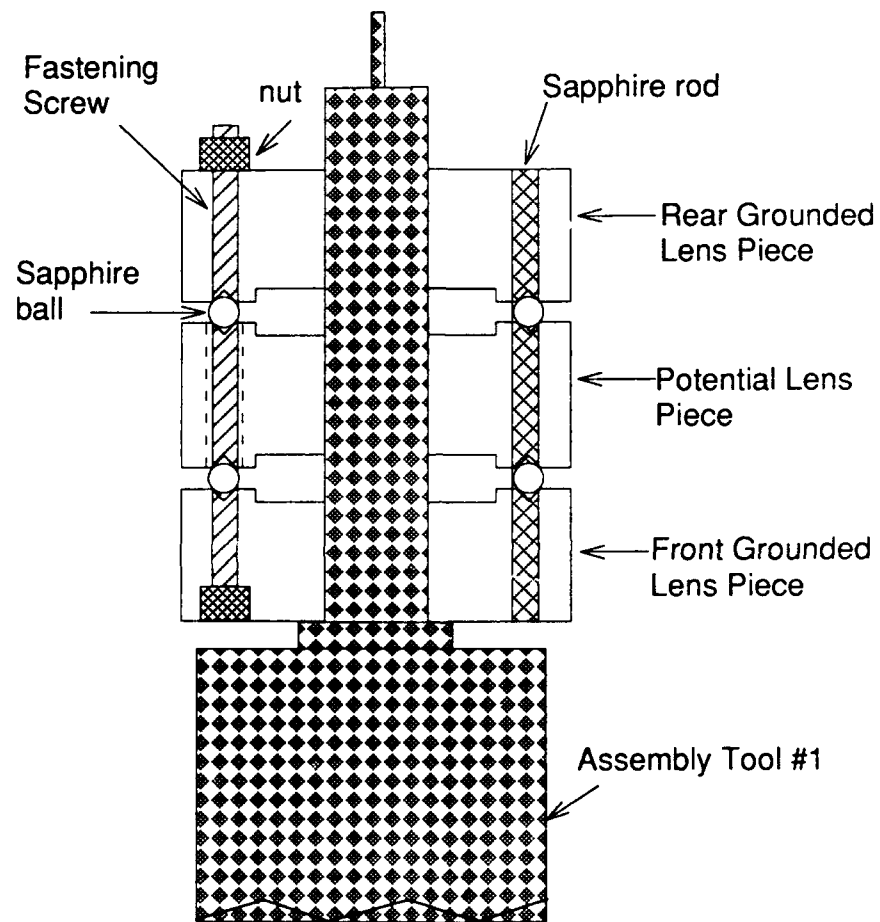


Figure 14: Assembly Method for E1, E3.

on this assembly tool for ease of alignment of the three component pieces of each lens. Since the shaft of Assembly Tool #1 was machined to fit snugly (within .001") into the lens openings of E1 and E3, it lends stability during their construction.

Place four Fastening Screws into the countersunk holes of the Front Grounded Lens Piece and place the center hole of this piece over the shaft of Assembly Tool #1. All four screws should be pointing toward the pointed end of the tool. Place two .060" diameter sapphire rods into their clearance holes. Now fill the groove with 1mm diameter sapphire balls. Carefully place the Potential Lens Piece over the Assembly Tool shaft and lower its appropriate clearance holes over the Fastening Screws or sapphire rod. The sapphire rods fix the two pieces rotationally about their lens openings to prevent the Fastening Screws from touching the Potential Lens Piece, thus providing electrical isolation between the lens pieces. The sapphire balls should be enclosed snugly between the grooves of the two lens pieces now stacked.

Fill the exposed groove of the Potential Lens Piece with 1mm diameter sapphire balls. Carefully place the Rear Grounded Lens Piece over the shaft of the assembly tool and lower its appropriate clearance holes over the Fastening Screws or sapphire rod. The clearance holes for the Fastening Screws provide a snug fit, providing an electrical connection between the Front and Rear Grounded Lens Pieces. Again the sapphire balls should be enclosed tightly between grooves. Now thread and tighten six nuts over the Fastening Screws. E1

construction is now complete and the entire lens may now be removed from Assembly Tool #1. Repeat this procedure to assemble E3.

Stage IV: Assembly of Steering Lens E2

To assemble E2 follow the procedures given above in Stage III with the following changes. Four sapphire rods are used instead of two to provide rotational stability for the four Biased Steering Lens Pieces (see Figure 10). Furthermore, it is helpful to place a small piece of foil into the gaps between each of the four Biased Steering Lens Pieces to prevent the sapphire balls from falling into these gaps during construction (see Figure 15). Do not remove these foil pieces until the nuts have been tightened down.

Stage V: Final Assembly of the Electron Optics

All the individual pieces are now completely assembled. It is time to place the Electron Gun, E1, E2, and E3 in their proper positions (both linearly and radially) in the Gun Housing. This is accomplished in the sequence shown in Figure 16. Once the steps in Figure 16 have been completed, both apertures of the Electron Gun and lens E1 are in their proper positions. To place E2 in its proper position, repeat steps 2, 3, and 4 of Figure 16, this time using Assembly Tool #2 (Figure 11). Similarly, to place E3, repeat the procedure using Assembly Tool #3. Since all the Assembly tools are machined to tolerances of plus or minus .001" in critical lengths shown in Figure 11, the procedure described above allows distances L1, L2, and L3 (Figure 1) to be achieved to the same tolerances. Furthermore, since the diameter of each Assembly Tool is at worst .003" less than

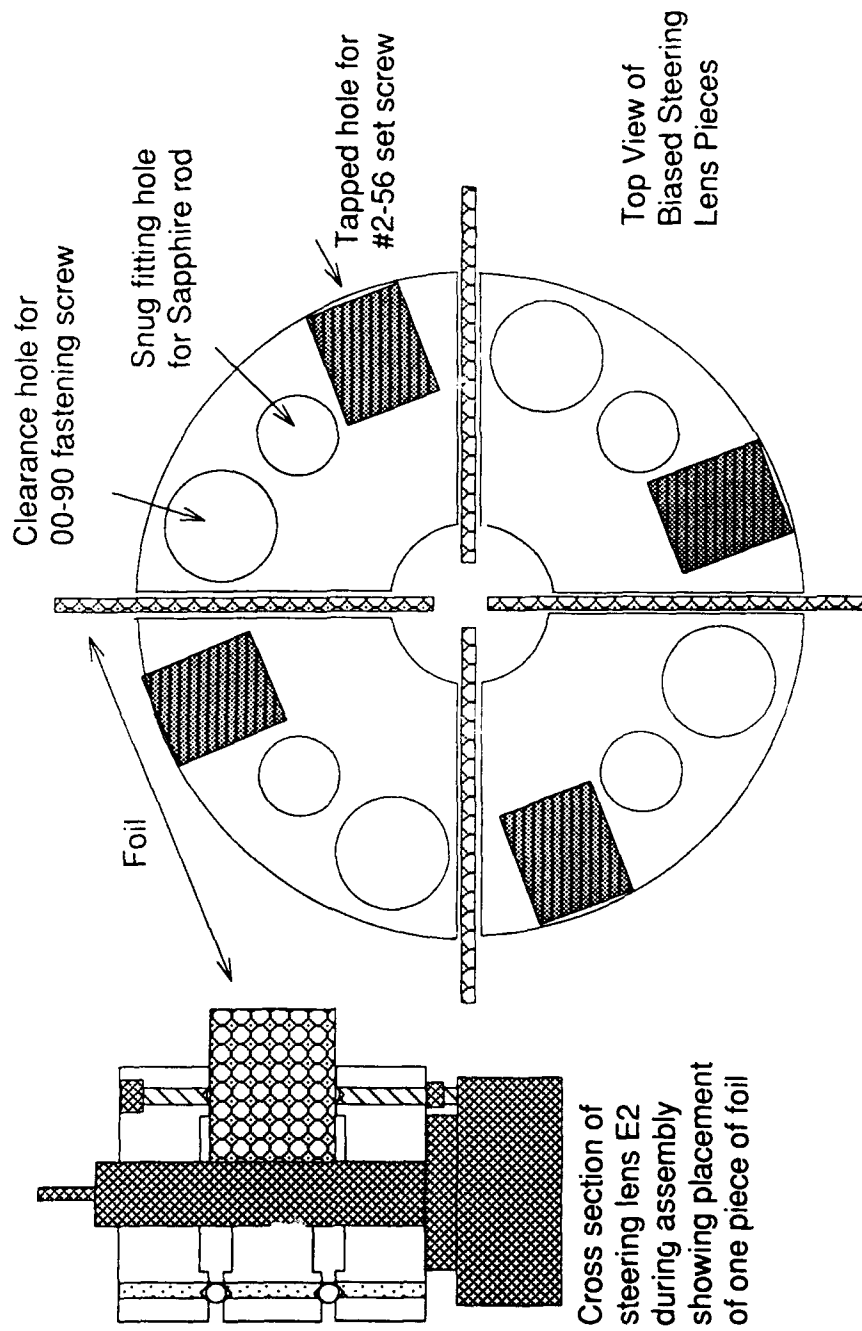
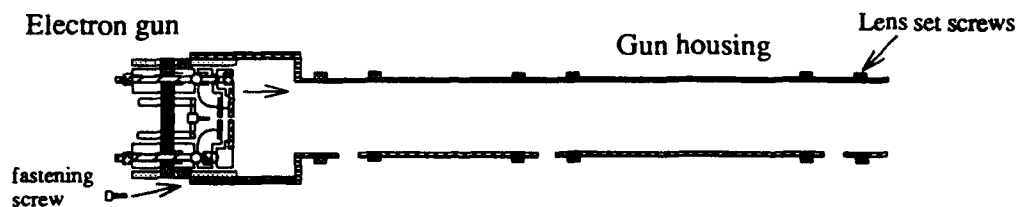
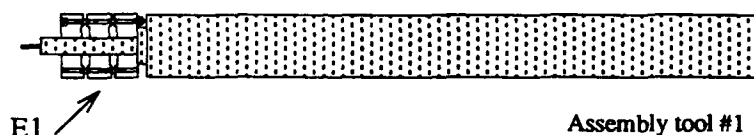


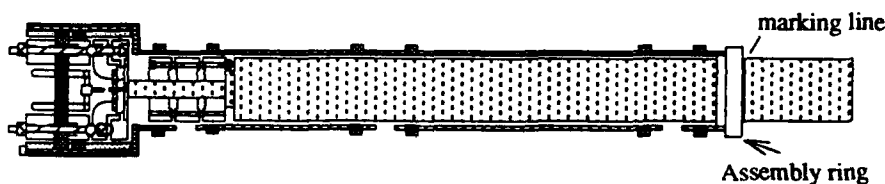
Figure 15: Assembly Of Steering Lens E2. Foil is used to prevent sapphire balls from falling into gaps between Biased Steering Lens Pieces during assembly.



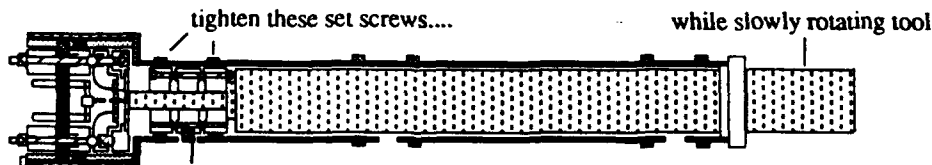
Step 1. After having completed construction of the electron gun, E1, E2, and E3, slide the electron gun into the gun housing and secure with the fastening screw. Insert all 36 lens set screws to be flush with the inside walls of the gun housing.



Step 2. Insert the shaft of assembly tool #1 through the center hole of the fully assembled E1 until it seats snugly. Make sure the protruding screws are away from the pointed end.



Step 3. Insert assembly tool #1 (with E1) into the gun housing. Slide the assembly ring onto the protruding end of the tool until it seats snugly between tool and gun housing. Then gently push the assembly tool until pointed end fits into electron gun apertures. This is done when the marking line is as shown.



Step 4. Rotate the assembly tool until the biasing hole of E1 can be seen through the clearance hole in the gun housing and insert the biasing screw/wire. Now carefully tighten all 12 set screws while slowly rotating the assembly tool, thus detecting any unwanted forces on the tool. Now slowly remove the assembly tool to leave E1 in its proper position.

Figure 16. Positioning E1 Using Assembly Tools.

its corresponding lens i.d., each lens E1, E2, and E3 can be placed within $(.003''/L1) = 11 \text{ mrad}$, $(.003''/[L1 + L2]) = 2 \text{ mrad}$, $(.003''/[L1 + L2 + L3]) = 0.8 \text{ mrad}$, respectively, of the optical axis defined by the center of aperture A2.

The final step is to attach a .015" diameter tungsten wire to the cathode and each aperture/lens. Connections are made as shown in Figure 7. For lenses A1, A2, and A3 a hole was spark cut into a #2-56 by 3/16" set screw to thread a tungsten wire through the set screw side of the hole and tie a knot on the opposite side. The wire is secured once the set screw is tightened down.

III. Power Control Unit

The power source for the electron optics consists of two parts: a commercially manufactured constant voltage supply and a power control unit. The commercial supply provides constant voltage which is divided and then directed to the lens elements, apertures, and LaB₆ cathode by the power control unit. The commercial voltage supply used throughout our tests was the Valhalla Scientific Model 2701C Programmable Precision DC Voltage Calibrator. This unit is capable of providing up to 1200V across its terminals in a floating mode with no more than 1.5 mV noise (14). The power control unit, besides being a voltage divider, also provides current to the LaB₆ cathode and metering of all pertinent information. This chapter will concentrate on providing the design requirements, design, testing, and operation of the power control unit.

Design Requirements

The design requirements of the power control unit were as follows:

1. Implement the unipotential design laid out by Cao and Conrad with the added feature of controlling the steering lens. This "unipotential" design takes a fixed input voltage V_s from the floating Valhalla supply into the power control unit voltage divider network. The LaB₆ cathode is biased negatively with respect to ground at a fixed fraction of V_s . This fraction furthermore referred to as V_{cathode} . V_{cathode} is solely a function of the *total* resistances of potentiometers used in the divider network and is not altered by changes in lens (aperture) voltage. Through manipulation of the divider network's variable potentiometers,

all other lenses E1, E2, E3 and apertures A1, and A2 are biased at a desired fraction of V_s . Now the focal length of each lens (aperture) scales as a ratio of $V_{lens}/V_{cathode}$ (2, 2642). Therefore, once the potentiometers have been adjusted to provide the minimum spot size, changing the value of V_s should only change the beam energy and not the focus. Cao and Conrad found in testing their gun that optimum focusing required the ratios of $V_{lens}/V_{cathode}$ as shown in Table 3. This Table shows that the maximum ratio required is that of $V_{E1}/V_{cathode}$, whose absolute value is 1.31. To provide for possible differences in our electron optics, we chose to design for 0-1.5 as our range of ratios for $|V_{(E1,E2,E3)}|/|V_{cathode}|$ and 0-1.0 as our range for $|V_{(A1,A2)}|/|V_{cathode}|$. Furthermore, to provide for reasonable beam energy for a given input voltage setting from the Valhalla voltage supply, we chose 0.4 as our desired ratio of $V_{cathode}/V_s$.

The steering lens' design requirements are twofold. First, it must behave like an einzel lens, just like E1 and E3. This means that all four center pieces of E-2 must be able to ramp up at the same voltage, call it $V_{E2 AVE}$. Second, opposite pieces of the center tube of E2 must allow controllable electrostatic deflection of the electron beam within the lens column. This should provide the capability to correct for any construction misalignment of the lenses (2, 2643). A differential steering voltage of 10% of $V_{E2 AVE}$, across the range of allowable values of $V_{E2 AVE}$, was the design goal.

2. Provide the power source and control for the filament current.

Table 3. Operating Parameters of the Lens and Electron Gun Elements as Provided by Cao and Conrad. All voltages are measured with respect to gun common, so that E1, E2, and E3 are biased positive with respect to ground, while A1, A2, and the cathode are biased negative with respect to ground.

Element	A1	A2	E1	E2	E3
$V_{\text{lens}} / V_{\text{cathode}}$	0.98	0.44	-1.31	0.0	-0.54

3. Provide continuous metering of filament and emission current while allowing external monitoring of cathode, lens, and aperture voltages from BNC connectors on the front and rear panel.

4. Limit the rms value of noise voltage at the cathode provided by the entire power source to less than 20mv. This value (in electron energy spread contribution) is less than 10% of the thermal energy spread of thermionic emission sources such as our LaB_6 cathode. Typical values for thermal energy spread fall between 0.2 and 0.6 eV, depending upon filament temperature (7, 2945).

5. Provide a retarding grid potential to the position sensitive detector which varies automatically with the cathode potential. This potential should be accessible by a rear panel BNC.

Design

To meet the design requirements 1 and 2, Figures 17, 18, and 19 show the basic circuit used. A "set and forget" (not controllable from outside the unit) 50Kohm potentiometer was used to achieve the designed maximum ratio of 1.5 for $V_{(E1,E2,E3)}/V_{\text{cathode}}$ while still maintaining V_{cathode}/V_s at 0.4. Its value from V_s to ground was adjusted to 29.78 Kohm. Table 4 shows a succession of equivalent circuits for ideal potentiometer values. It shows that the position of the 20Kohm steering potentiometers for E2 has little effect on the ratio V_{cathode}/V_s or $V_{(E1,E2,E3)}/V_{\text{cathode}}$. The steering lens portion of the circuit required two dual 200Kohm potentiometers interconnected in phase through a 1:1 ratio gearbox to ramp up the voltage on all four biased pieces of E2 simultaneously. Two

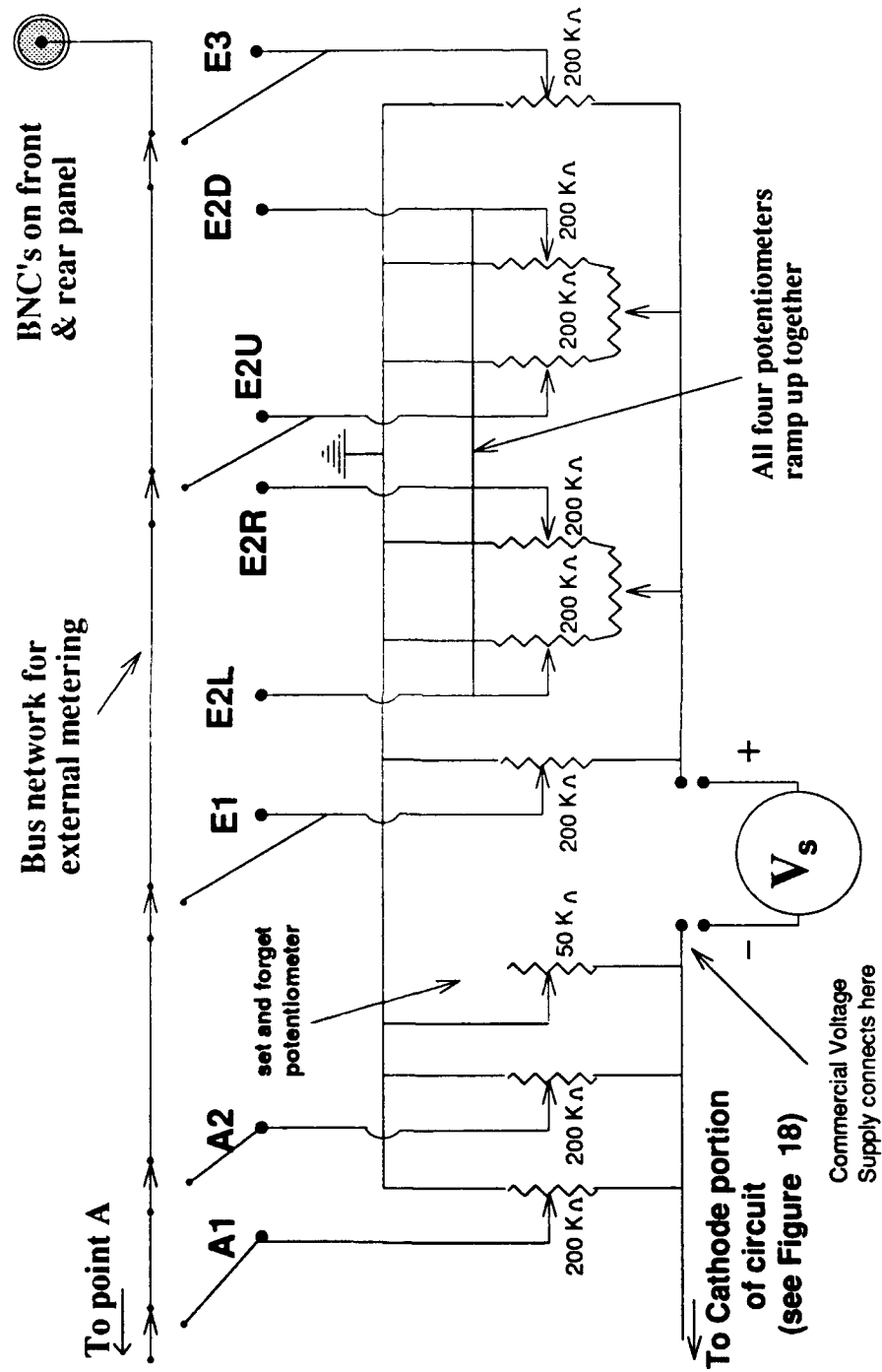


Figure 17. Circuit Diagram for Voltage Divider Portion of Power Control Unit

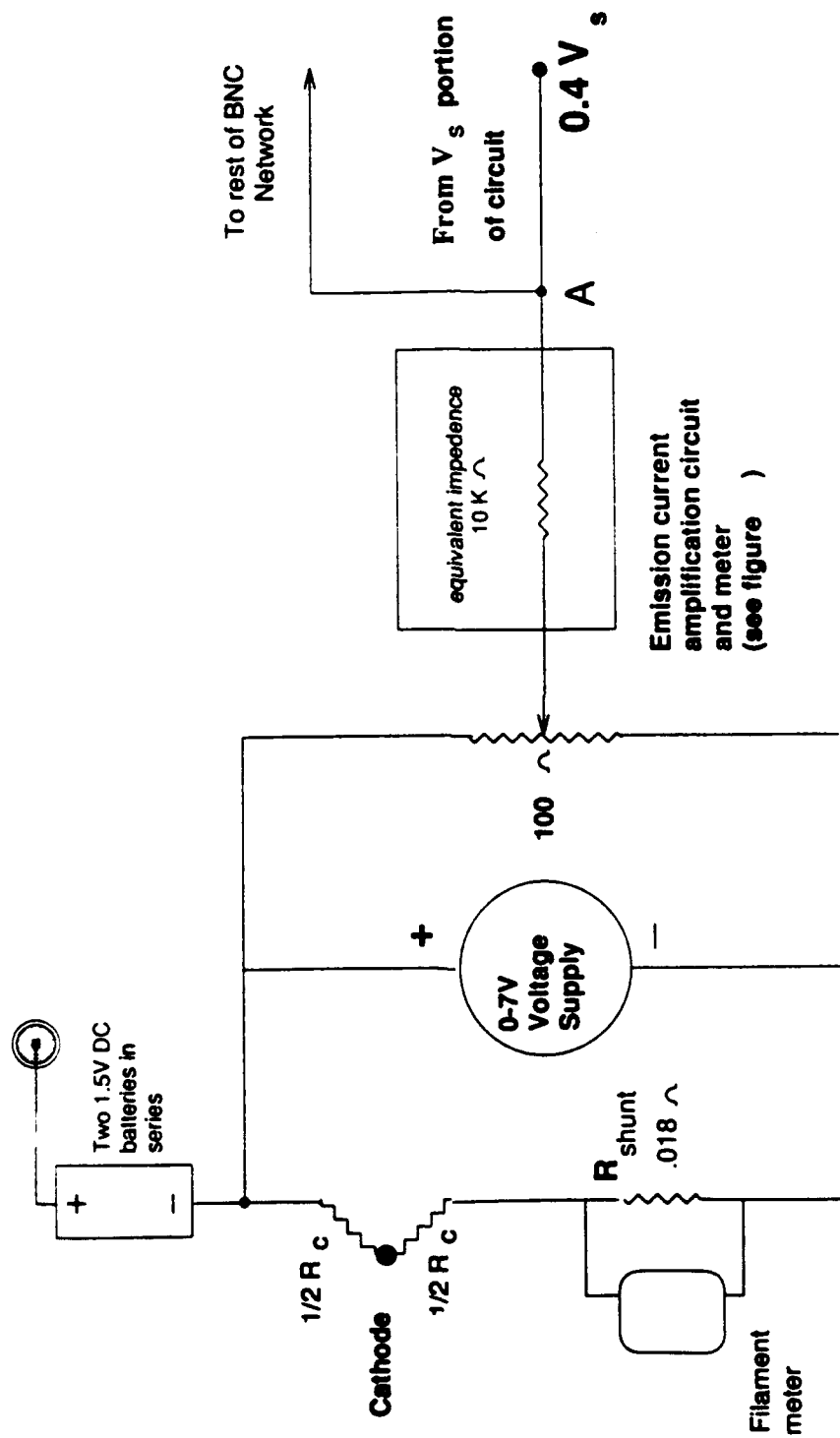


Figure 18. Circuit Diagram for Cathode Portion of Power Control Unit

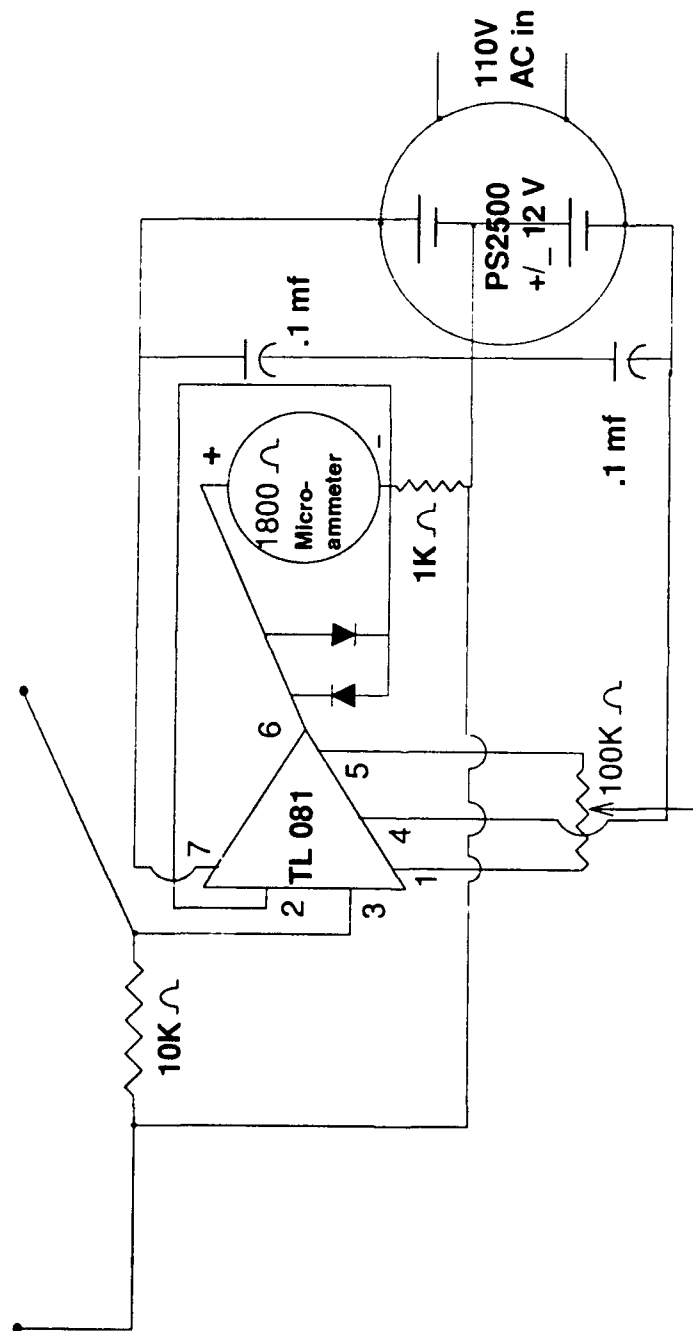
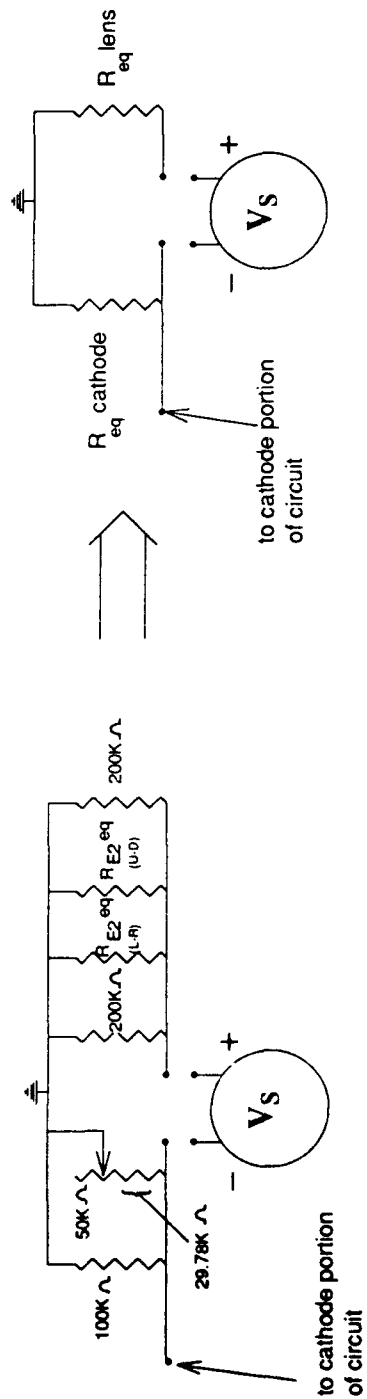


Figure 19. Amplification Circuit for Emission Meter



Position of 20 K Ω pots	Value of R_{E2}^{eq} left-right	Value of R_{E2}^{eq} up-down	Value of R_{eq}^{lens}	Value of $R_{eq}^{cathode}$	Potential across $R_{eq}^{cathode}$	Max ratio $V_{E3}/V_{Cathode}$
Both centered	105.0 K	105.0 K	34.43K	22.95K	-.4000 Vs	-1.500
Both full deflection	104.8 K	104.8 K	34.37K	22.95K	-.4004 Vs	-1.498
One full deflection, one centered	104.8 K	105.0 K	34.40K	22.95K	-.4002 Vs	-1.499

Table 4. Equivalent Circuits of Voltage Divider Portion of Power Control Unit

20Kohm potentiometers, chosen because this value should allow 10% differential voltage between opposite pieces.

The power source for the filament current is a Lambda LDS-Y-01 0-7V constant voltage source. It is rated at 150 microvolt rms, 1 mV peak to peak noise, well below what we have set for our noise limit (12). Changes in voltage, therefore filament current, are affected through manipulation of a 50Kohm potentiometer from the front panel. This potentiometer is connected according to instructions in the Lambda manual.

Continuous metering of filament and emission current is provided by two 0-50 mV full scale deflection analog ammeters on the front panel. Full scale deflection of the 1800 ohm filament meter has been adjusted to 5 amps by a .018 ohm shunt resistor in parallel. This resistor was made of 20 gauge copper bus wire wound around a cylinder of Teflon. Calibration is achieved by varying the length of the wire. Full scale deflection of the 1800 ohm emission meter was adjusted to 5 microamperes by the use of the 10-gain amplification circuit shown in Figure 18. Calibration is achieved through manipulation of the 100Kohm potentiometer shown.

External monitoring of the cathode, lens, and aperture voltages is achieved by connecting a voltmeter to one of two BNC's provided (front and rear panel). These BNC's are connected to a bus system of 3 position switches shown in Figures 17 and 18. The system is wired so that the BNC is nominally at potential $0.400V_s$. The 100 ohm resistor has been adjusted so that the center of the cathode is at the monitored value ($0.400V_s$) less a correction on the order of 20

millivolts due to the emission current flowing through the circuit. For further details see the **Testing** section. Upon pressing the appropriate push button on the front panel, the external voltmeter will read the exact potential of all the lenses. Notice that the voltage read externally for E2 is really that of E2U.

Noise limitation was attempted by twisting and shielding all AC power lines. No filtering of the Lambda or emission meter amplification circuit was needed to reach the design goals. Finally, the retarding grid potential is always approximately 3V less in magnitude than the gun potential due to the two 1.5 DC batteries connected as shown in Figure 18.

Testing

To determine the true ratios of $V(E1,E2,E3)/V_{cathode}$ and $V(A1,A2)/V_{cathode}$ it is necessary to determine $V_{cathode}$ accurately. To do this, a 5 ohm load was placed across the cathode output terminals of the 20 pin amphenol connector to simulate the cathode resistance. One ampere was passed through this load. The 100 ohm potentiometer (refer to Figure 18) was adjusted until the average potential across the 5 ohm load was equal to the voltage at point A (measured to be $0.400V_s$) within the limits of accuracy of the multimeter, .001 volt. The position of this potentiometer was locked at the control knob. Therefore, *without any emission current flowing*, the potential at the center of the cathode is $0.400V_s$, the nominal value of the test BNC's. However, when emission current is flowing during actual operation, the true value of $V_{cathode}$ will be equal to $\{V_{cathode\ metered} - (I_{emission})(10Kohm)\}$. At typical operating emission currents of 2 microamps, this correction is of the order of 20 millivolts. Metered values of the

lens and aperture voltages need no correction. Table 5 shows the actual available ratios of $V(E1,E2,E3)/V_{\text{cathode}}$ and $V(A1,A2)/V_{\text{cathode}}$ as measured.

The four 200Kohm steering lens resistors were connected in phase at 0.000 ohms. However, due to slight inherent non-linearities, they ramp up with a variation in resistance among them which never exceeds 0.5% throughout the entire range of resistances. The voltage differential available across E2L/E2R and E2U/E2D were measured to have absolute values of 0 to 10% of $V_{E2 \text{ AVE}}$.

Voltage noise at the cathode was measured on an oscilloscope with the Valhalla power supply providing input voltages in 100 volt increments to 1000V. Peak to peak values never exceeded 20 mV, therefore the rms value never exceeded 4 mV (5, 454). This value is well below our design standard, ensuring that the energy spread of the beam will be dominated by the thermal energy spread of the LaB₆ cathode.

Operation

Operation of the power control unit is straightforward. Refer to Figure 20. **Power Control Unit Rear Panel.**

1. AC power is applied here. AC power is necessary for the fan, emission current meter amplification circuit, and Lambda voltage supply.
2. Fuse. A 3 amp fuse is currently installed.
3. $V_{s \text{ in}}$. This is an insulated input since the Valhalla power supply must be connected to the power control unit in the floating mode.

Table 5 . Available Ratios of $V_{\text{lens}} / V_{\text{cathode}}$ as Measured With Input Voltages Ranging to 1000 Volts. All voltages are measured with respect to gun common, so that E1, E2, and E3 are biased positive with respect to ground, while A1, A2, and the cathode are biased negative with respect to ground.

Element	A1	A2	E1	E2	E3
$V_{\text{lens}} / V_{\text{cathode}}$	0.000 -	0.000 -	0.000 -	0.000 -	0.000 -
	1.000	1.000	-1.498	-1.425	-1.497

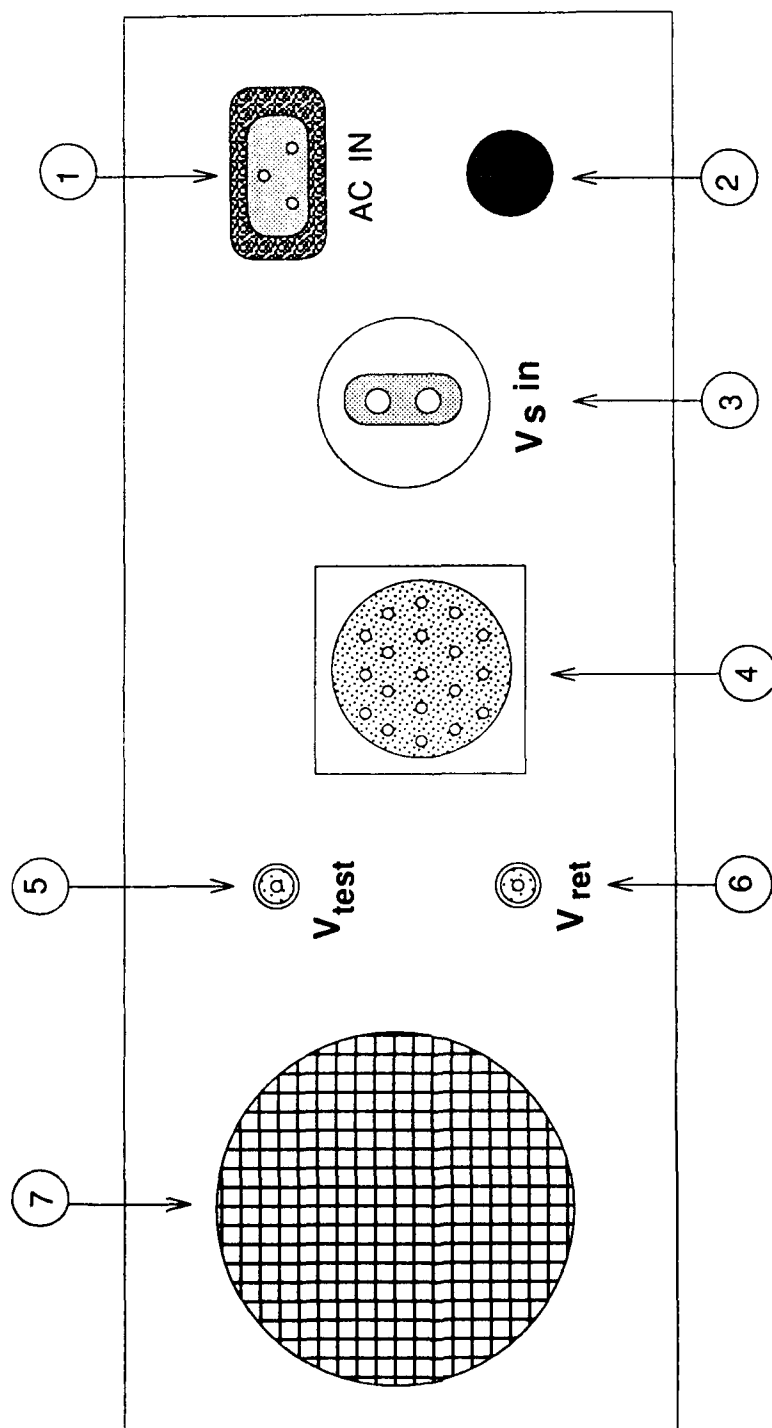


Figure 20. Power Control Unit Rear Panel

4. This amphenol 20 pin connector allows application of all aperture, lens, and cathode potentials and filament current to the electron optics. Figure 21 shows the pin connections at both sides of the shielded cable used.

5. V_{test} . This is one of two BNC connections (the other is on the front panel) to the bus network which allows external monitoring of lens, aperture, and cathode potentials. The nominal value of the potential of this BNC is approximately V_{cathode} .

6. V_{ret} . This BNC connector provides the retarding grid potential to the position sensitive detector.

7. This is the screened ventilation hole for the electric fan. This fan is always in operation when the unit power switch is on.

Refer now to Figure 22, **Power Control Unit Front Panel**.

1. Emission meter, 0-5 microamps full scale.

2. Filament meter, 0-5 amps full scale.

3. Power switch. Turn the switch up toward the stencil "pwr" to apply AC power. This switch must be on to provide filament current.

4. V_c adjust. This ten turn potentiometer knob adjusts the 100 ohm resistor shown in Figure 18, affecting the measure of V_{cathode} . It is currently locked in the center position.

5. I_c . This ten turn potentiometer knob adjusts the voltage applied across the filament, varying from 0 to 7 volts clockwise.

6. This is one of two BNC connections (the other is on the rear panel) to the bus network which allows external monitoring of lens, aperture, and cathode

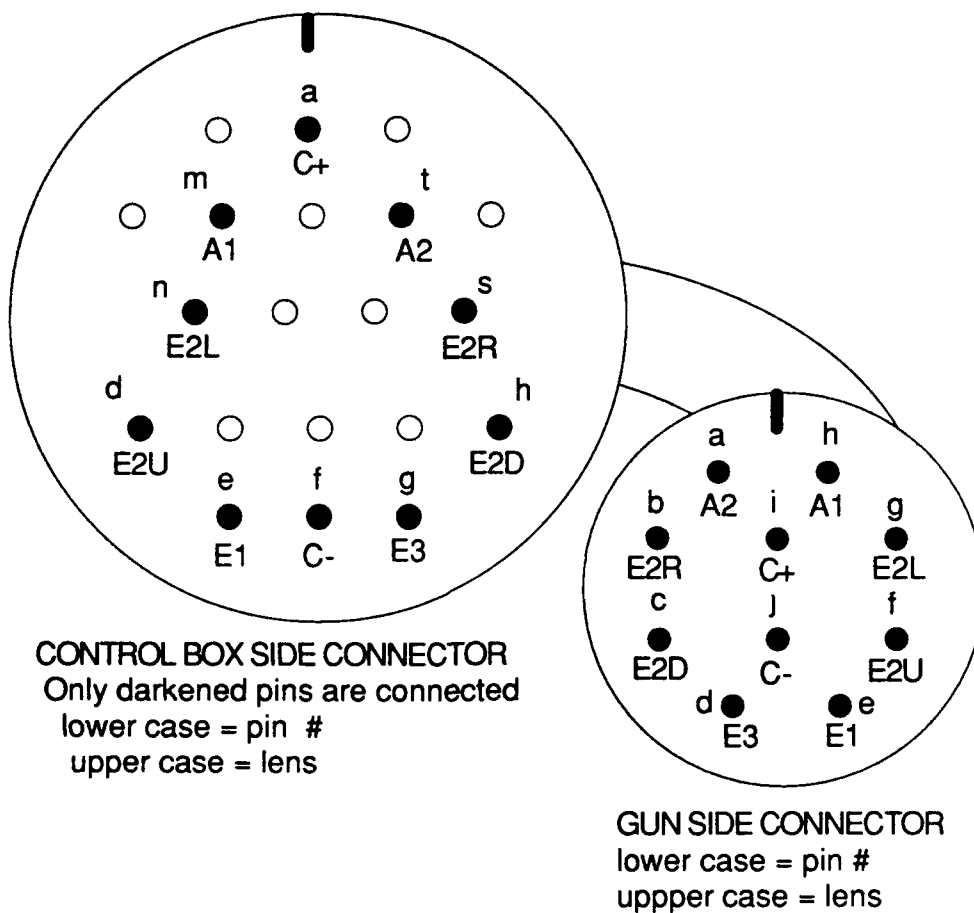


Figure 21. Pin Connections for Cable Connecting Power Control Unit to Electron Optics.

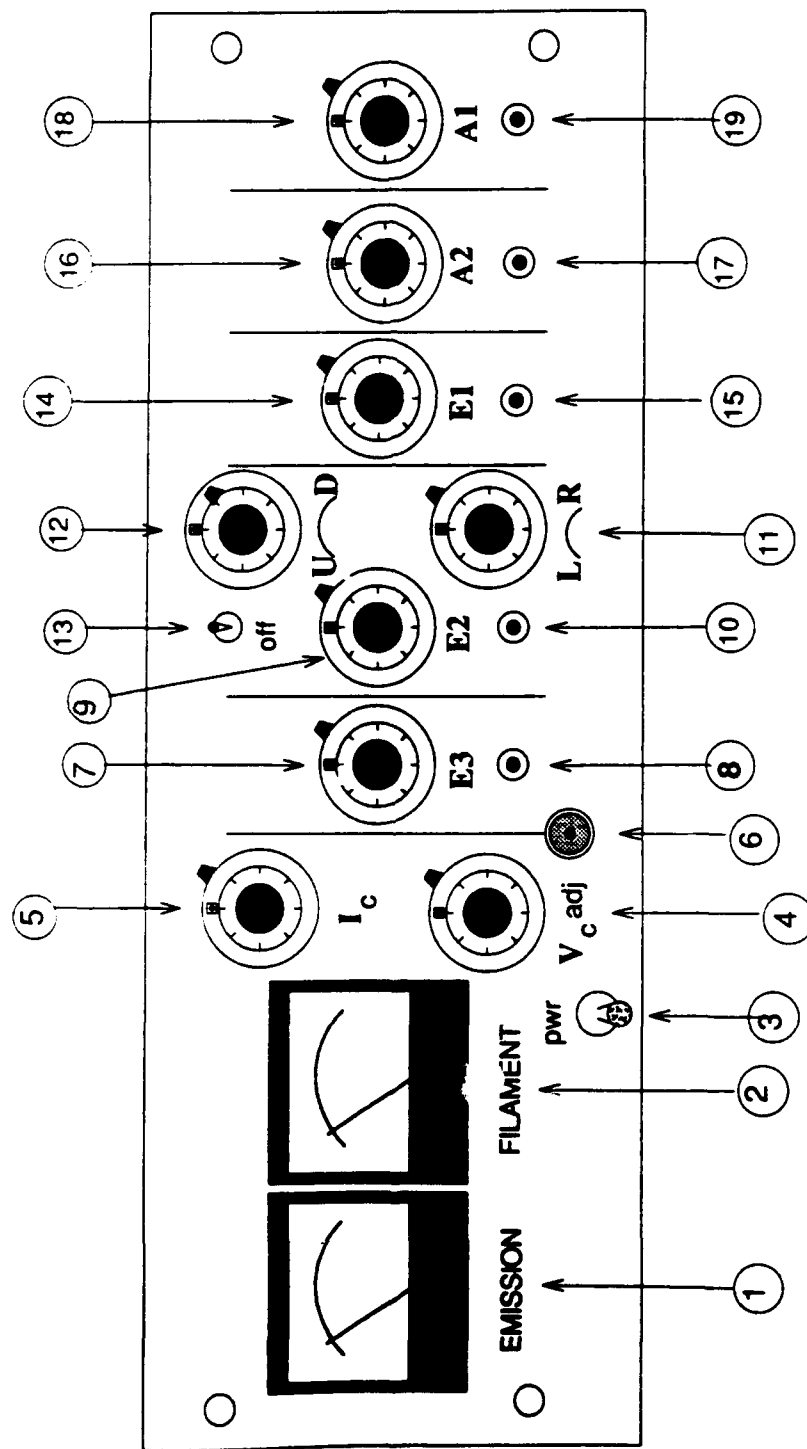


Figure 22. Front Panel of Power Control Unit.

potentials. The nominal value of the potential of this BNC is approximately V_{cathode} .

7. This ten turn potentiometer knob adjusts the voltage applied across E3, varying from 0 to $.598V_s$ in clockwise.

8. This pushbutton, when held in, places the test BNC's on front and back panels at V_{E3} .

9. This ten turn potentiometer knob adjusts the voltage applied across the four biased pieces of E2, varying from 0 to $.570V_s$ in clockwise.

10. This pushbutton, when held in, places the test BNC's on front and back panels at V_{E2U} .

11. This ten turn potentiometer knob adjusts the wiper on the 20Kohm steering lens resistor which steers the beam left (referenced on the flange upon which the electron gun is mounted) if rotated counterclockwise and right if clockwise.

12. This ten turn potentiometer knob adjusts the wiper on the 20Kohm steering lens resistor which steers the beam up (referenced on the flange upon which the electron gun is mounted) if rotated counterclockwise and down if clockwise.

13. This toggle switch, when toggled down toward the stenciled "off", places all four biased pieces of E2 at ground.

14. This ten turn potentiometer knob adjusts the voltage applied across E1, varying from 0 to $.599V_s$ in clockwise.

15. This pushbutton, when held in, places the test BNC's on front and back panels at V_{E1} .
16. This ten turn potentiometer knob adjusts the voltage applied across A2, varying from 0 to $-.400V_s$ in clockwise.
17. This pushbutton, when held in, places the test BNC's on front and back panels at V_{A2} .
18. This ten turn potentiometer knob adjusts the voltage applied across A1, varying from 0 to $-.400V_s$ in clockwise.
19. This pushbutton, when held in, places the test BNC's on front and back panels at V_{A1} .

IV. Experimental Method

In Section I, the major factors which contribute to beam broadening were discussed to provide rationale for choosing our electron optics system. However, to measure the transfer width of a LEED instrument experimentally it is not necessary to independently measure the contribution to the instrument response function from each of these factors. Instead, remembering that

$$i(\mathbf{k})_{\text{meas}} = i(\mathbf{k})_{\text{true}} * T(\mathbf{k}),$$

and that the intensity profile from a perfectly ordered, flat surface should be delta function diffraction spots, it can be seen that recording a spot intensity pattern from a well ordered, flat surface will give the approximate response function $T(\mathbf{k})$ of the LEED instrument (16, 64). Assuming Gaussian distributions, one can then use the equations in Section I to calculate the approximate transfer width t . For measurements on the specular beam, this transfer width t is given by:

$$t = \lambda / (\text{FWHM } \Delta\theta) \cos\theta_0$$

where $\Delta\theta$ is the measured angular width of the specular electron beam at the detector, θ_0 is the angle of incidence the incident electron makes with the sample normal, and λ is the wavelength of the electron with energy E (2, 2644). Figure 23 shows the reciprocal space scattering geometry for a specular beam

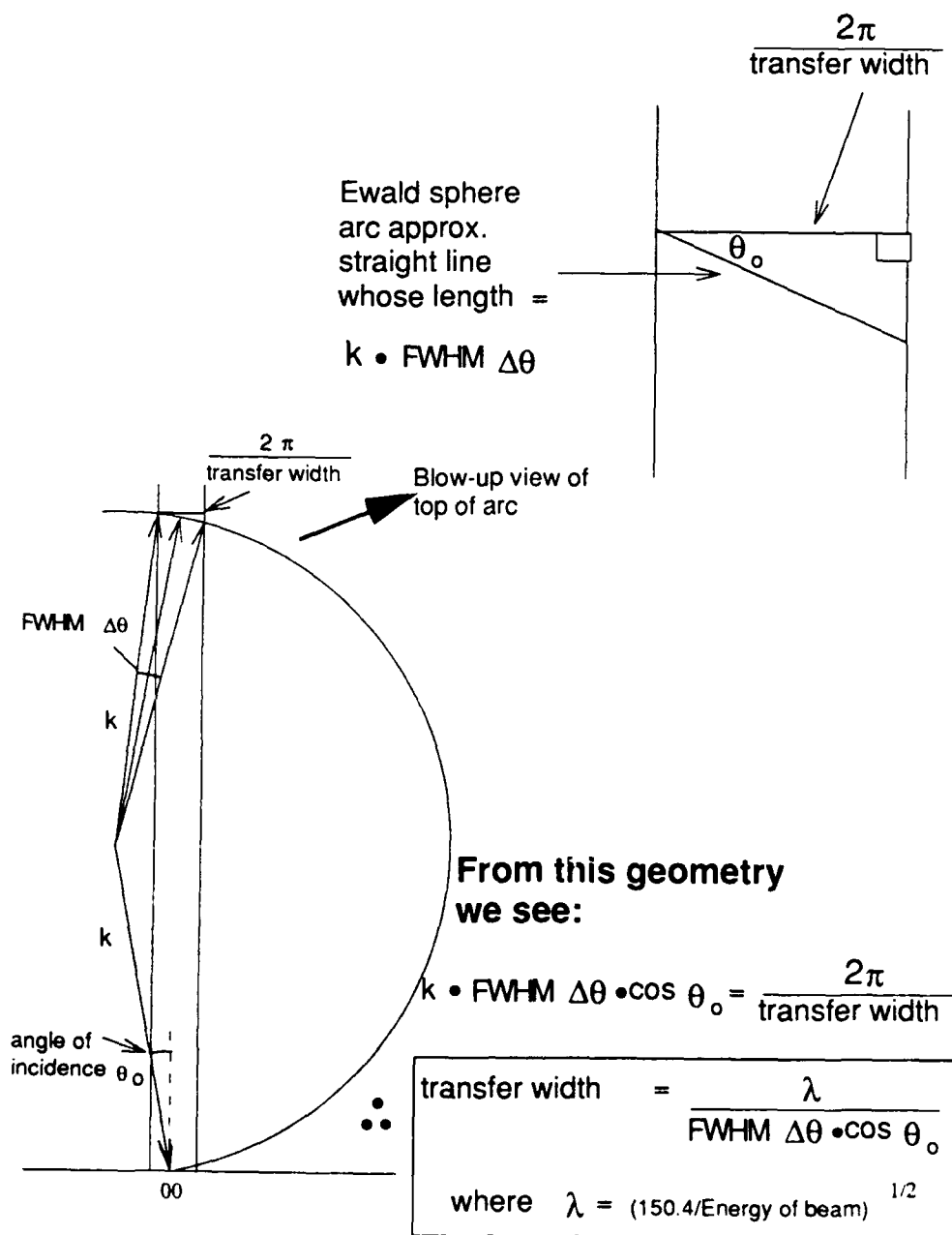


Figure 23. Measuring the Transfer Width. This diagram shows the reciprocal space broadening of a surface rod we measure. Assuming a flat surface, all the broadening is due to the instrument and the real space transfer width is deduced from this geometry.

measurement and the derivation of the above equation. It is evident that the parameters one needs to know to measure the transfer width experimentally are the *beam energy*, the *FWHM of the angular spread* of the diffracted beam at the detector, and the *angle of incidence of the beam*. The remainder of this section describes the apparatus and techniques used to make these measurements, and reports some rough estimates of the system performance.

Experimental Apparatus

Figures 24 and 25 show schematics of the experimental apparatus. Figure 24 shows the overall picture of the equipment used. Figure 25 shows the geometrical arrangement of the electron optics, sample, and detector. The electron optics and detector are both secured to a 6 inch conflat flange which mates to a 4 in o.d., μ -metal shielded stainless tube extension. This tube extends the distance from the inside edge of the flange to sample to 11.25 in, allowing us to achieve a 10.5 in distance from sample to detector as shown. The electron optics are mounted on a track system (itself secured *only* to the 6 in flange) which points the optical axis at an 8 degree angle (measured from flange normal) toward the sample center. This track system allows a linear motion feedthrough to manipulate the optics/sample distance through a continuous range from 2.29 to 3.98 inches. Table 6 shows the distances from the center of lens E3 to the sample as a function of the number of turns counterclockwise from full forward extension of the linear motion feedthrough. This linear freedom allows us to match the focal length of lens E3, which, at optimal focus settings, Cao and Conrad reported as 2.51 inches (2, 2643). Fiberglass-shielded wires from the electron optics are

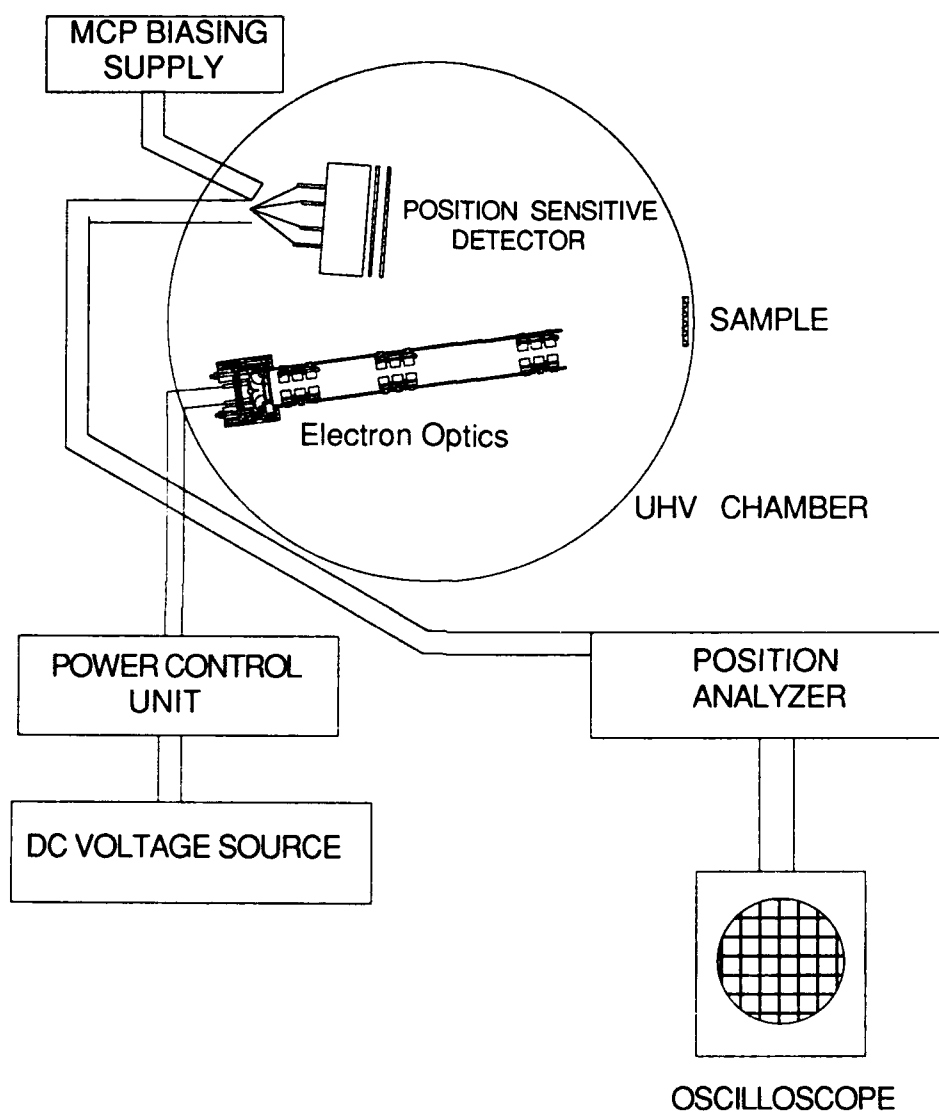


Figure 24. Schematic of the Experimental Apparatus. A more detailed look at the optics-sample-detector geometry is shown in Figure 25.

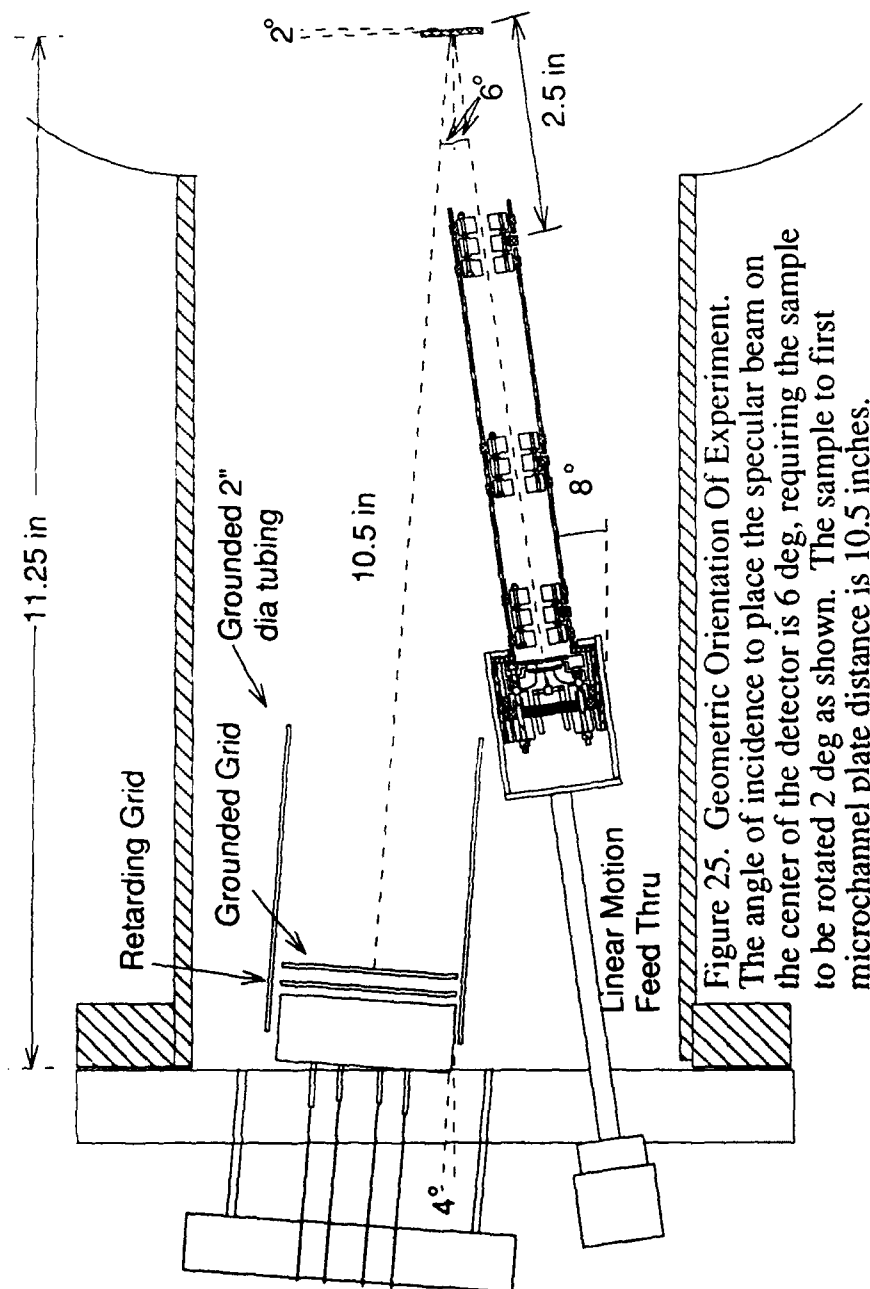


Figure 25. Geometric Orientation Of Experiment.
The angle of incidence to place the specular beam on the center of the detector is 6 deg, requiring the sample to be rotated 2 deg as shown. The sample to first microchannel plate distance is 10.5 inches.

Number of turns from full forward extension (etched lines coincide)		Distance from center of E3 to sample + or - .1 in
0		2.29 in
1		2.32
2		2.35
3		2.38
4		2.41
5		2.44
6		2.47
7		2.50
7.33		***2.51***
8		2.53
9		2.56
10		2.59
15	Each turn moves optics .03 in.	2.74
20		2.89
25		3.04
30		3.19
35		3.34
40		3.49
45		3.64
50		3.79
54.5 full aft		4.00

Table 6. Sample to E3 Distances. The asterisks mark the focal length published by Cao & Conrad.

routed through the same feedthrough which routes electrical leads to the position detector. A grounded .050 inch thick stainless steel sheet blankets the entire side of the electron optics to shield the diffracted electron path from electric fields generated by the high voltage electron optics leads.

The sample used for these tests is our best candidate for the theoretical perfectly flat, well-ordered surface. It is a silicon single crystal whose surface is oriented to within .05 degrees of the (111) plane, thus giving a terrace width of approximately 4000 angstroms. This crystal is held via a molybdenum mount on a standard UHV manipulator which provides azimuthal, translational, and rotational motion. A tungsten filament is suspended behind the crystal to provide the source for electron beam heating.

The detection system used in this experiment consists of a 25mm active area, 5 microchannel plate/resistive anode (MCP/RAE) position sensitive detector. This detector is connected to a position analyzer which outputs to an oscilloscope for real time display of individual electron events at the detector. In operation, incident electrons strike the front surface of the first microchannel plate, resulting in secondary electron production from the wall of one or more microchannels (13). Because of an applied electric field between the 5 microchannel plates, an electron avalanche occurs with a gain of approximately 5×10^7 . The resulting charge cloud from the fifth microchannel plate travels in a uniform electric field and strikes the resistive anode encoder (RAE) with its centroid at the same position as the incident electron. This charge packet then diffuses in the uniform resistive sheet of the RAE to be collected by four metallic contacts at the corners of

the sheet. The relative charge reaching each of the four contacts is a linear function of the position of the incident electron on the X and Y orthogonal axis of the RAE. This position is then decoded by the position analyzer.

The spatial resolution of this detector is rated at 1/400 of the active area diameter of 25mm, thus 2.5×10^{-3} in. (13). The angular resolution for our detector, which is mounted 10.5 in from the sample, is thus $[(2.5 \times 10^{-3})(180)] / (10.5)(\pi)]$ deg or .014 deg. The width of the pattern intercepted by the active area of the detector is 5.37 deg. The maximum digital output data rate of the system is 60 KHz and is limited by the position analyzer.

The information from the position analyzer can be displayed *simultaneously* as a real-time oscilloscope image of the position detector *and* digitally via a computer. Ideally, both displays would be used: the oscilloscope for real-time *qualitative* information and the computer for a digital, two dimensional (1024 channels x 1024 channels) *quantitative* mapping of the detected events. The digital representation is ideal for SPA-LEED because the quantitative digital information can be readily analyzed. Unfortunately, at the time of this report, we are still working on the interface between the position analyzer and a Mac IIfx computer. Therefore, all reported data from the position detector in this report has been gleaned from an oscilloscope.

The MCP/RAE detector has been fitted with two grids made from 85% transmission stainless screen to deter inelastic electron detection. These screens are sandwiched between stainless rings which are attached to the front face of the detector. Referencing Figure 25, the grid closest to the sample is grounded while

the one closest to the first MCP is biased approximately 3 volts above any selected electron gun cathode voltage via the circuitry described in Section III. Shielding of the uniform field region between the five microchannel plates and the RAE from electric fields caused by the high voltage electron optics connections is achieved by connecting an electrically grounded, 2 inch o.d. stainless steel tube to the ceramic base of the MCP/RAE detector. This tube extends 2 inches toward the sample from the RAE.

The final modification to the MCP/RAE detector is a stainless shield with a .002 inch wide slit in it attached to the front grounded grid ring. This apparatus is shown in Figure 26. Its purpose is to allow measurement of the width of the diffracted beam by rastering (by electric deflection provided by E2) it across this slit.

The position sensitive detector, electron optics, and sample are all enclosed in a stainless steel, μ -metal sleeved, ion pumped UHV chamber which is equipped with an Auger electron spectrometer, a commercial Varian LEED electron gun and phosphor screen. This chamber was capable of maintaining pressures in the high 10^{-10} to low 10^{-9} Torr range throughout the experimental procedure.

Experimental Procedure

To make the measurements required to determine the transfer width of the system, we used the following procedure. Once all components were under vacuum (high 10^{-10} to 10^{-9} Torr) and all filaments had been outgassed, the silicon sample was cleaned by electron beam heating. The sample was maintained

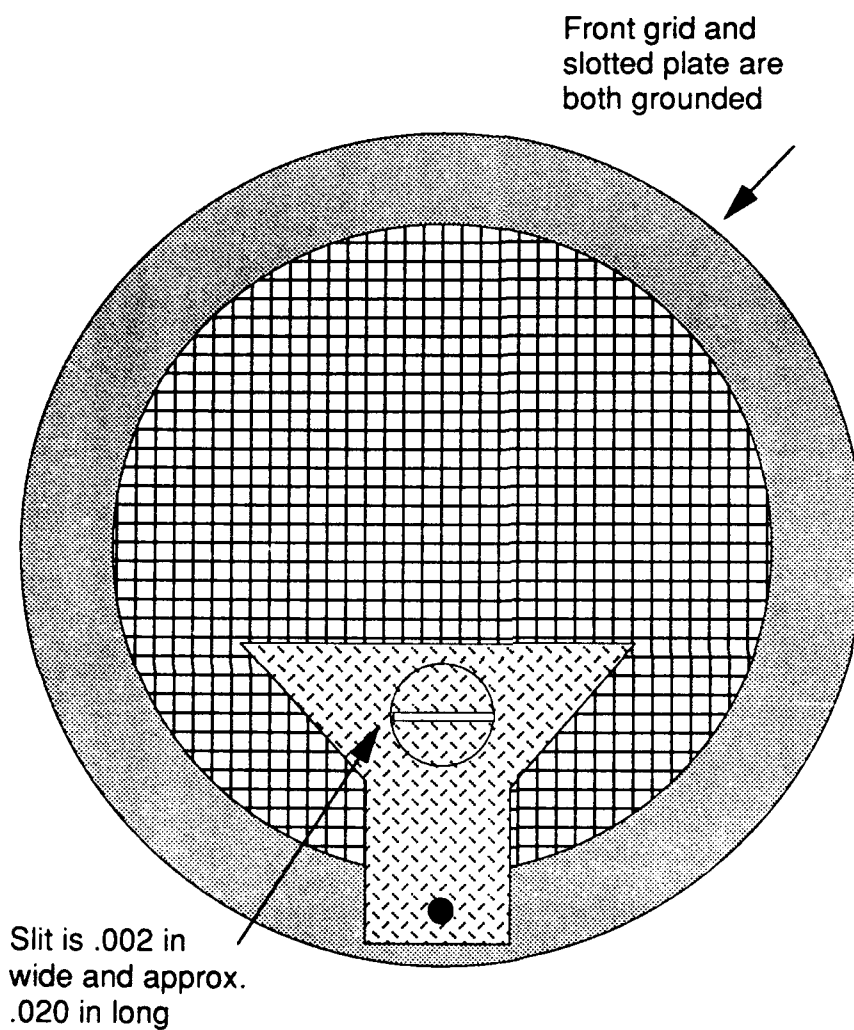


Figure 26. Front Grid of MCP/RAE Detector. This view shows the slit which was attached to the front grounded grid ring. It was hoped measurement of the angular width of the diffracted beam could be achieved by rastering the beam across the slit.

at approximately 1100 degrees C for 15 minutes, then cooled at a rate of approximately 1 degree/second down to ambient temperature. This cycle was repeated until we got a sharp (7 x 7) reconstruction pattern on the phosphor screen from the Varian LEED gun. A sample of this detected pattern, which has been photographed, digitized, and computer processed is shown in Figure 27. With the sample cleaned, the position sensitive detection system was brought to life. Following the Quantar Technology instruction manual, the factory bench-tested high voltages (front MCP at ground potential) were applied to the five microchannel plates and the RAE (13). Also per instructions, the oscilloscope was connected, powered up, and adjusted. At this point, the circular image of the MCP was discernable from random counts *and* from ion gauge counts. The image has a diameter equal to the full oscilloscope screen width. It was found that the ion gauge had to be turned off during testing because it caused excessive background counts. Next, the electron optics were powered up via the power control unit and Valhalla supply. The LaB₆ filament was allowed to warm up for 15 minutes at 1.4 amperes filament current according to manufacturer's recommendation (11).

We were now ready to commence measuring the angular spread of the specular beam at the detector for various gun energies. However, with a limited time available to carry out these tests, the question of how to minimize the beam spread as a function of all the lens voltages (A1, A2, E1, E2U, E2D, E2L, E2R, and E3), the filament current, and the distance from the last lens element (center of E3) to the sample needed to be addressed. Fortunately, focal length scaling

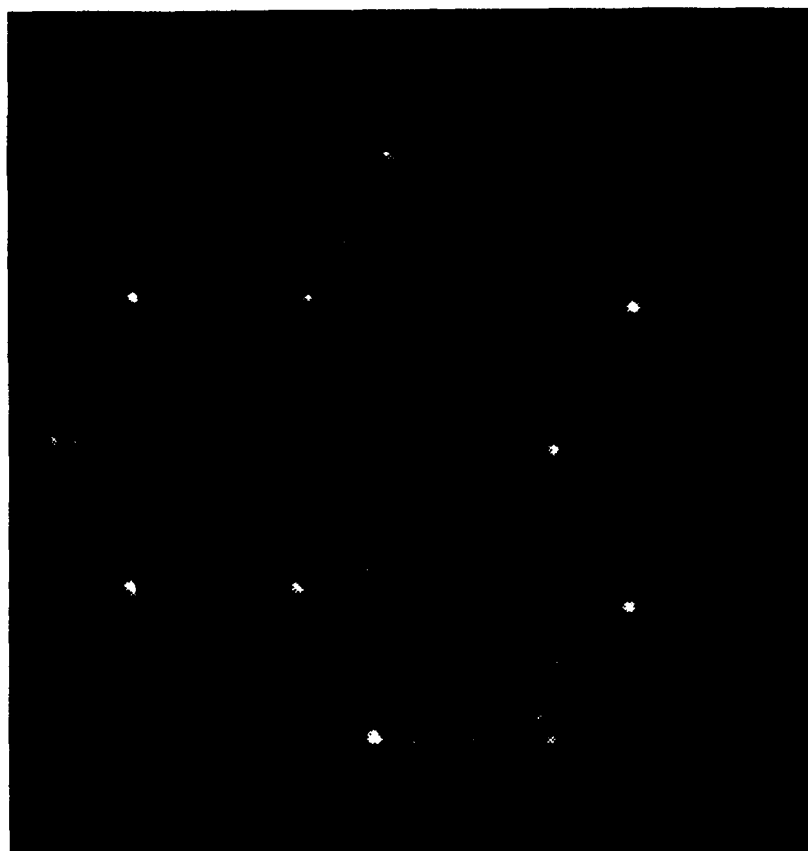


Figure 27. LEED Pattern of Si (111) From Commercial System at 100 eV.

should make optimizing the lens voltages a one time job, independent of the beam energy. However, with so many variables and limited time, some parameters had to be fixed and a systematic scheme had to be followed when changing the others.

Fortunately, we had the published test results from Cao and Conrad to use as a **starting point** (2, 2642). To eliminate one variable *throughout* the tests, the electron optics were positioned, via the linear motion feedthrough, so that the center of E3 was 2.51 inches (\pm 0.1 inches) from the sample. This distance is the focal length of lens E3, at optimal focus settings shown in Table 3, published by Cao and Conrad (2, 2643). Furthermore, we began all tests with the lens voltage ratios $V_{\text{lens}}/V_{\text{cathode}}$ set at the published values shown in Table 3. This included setting all parts of E2 to ground. We also began all tests with the filament current set at 1.4 amps, corresponding to the 1650 K cathode temperature which Cao and Conrad found optimum (11), (2, 2643).

With these initial parameters set, the sample orientation was adjusted until the specular beam was located on the oscilloscope for the given beam energy under study. Since for energies below approximately 100eV only one spot was discernable on the oscilloscope, confirmation of the beam as specular was done by noting no change in position upon beam energy change. Once we confirmed the *specular* beam on the scope, the first parameter we adjusted was the *filament current*. Filament currents below approximately 1.3 amps failed to produce a diffracted beam on the detector (remember we were maintaining constant biasing of the MCP's and RAE, therefore fixed gain). It was found that currents higher than 1.4 amps increased the background counts significantly and saturated the

pixels comprising the specular spot, yet did nothing to minimize the visually determined spread of the beam. In fact, for beam energies below 80 eV, increasing the filament current above 1.4 amps caused further beam spreading. For the remainder of the tests the filament current was adjusted to 1.4 amps when attempting to minimize the FWHM $\Delta\theta$.

Next, with the other lens values still at initial parameters, we began to experiment with the steering lens E2 to see if it could deflect the beam enough to make the slit measurement technique possible. First, we began by ramping up the average voltage of E2 with all other lens voltages constant. Then, once we found the value of $E2_{ave}$ which minimized the spot size, we began adjusting the potential difference across opposite pole pieces of E2 (LEFT-RIGHT, UP-DOWN) to find the minimum spot size. What was observed was a noticeable decrease in intensity of the specular spot when the steering potentials were full scale. Furthermore, a particular setting (reported later in Table 7) produced a more spherical spot on the detector and minimized the spot size. However, the steering lens was found incapable of rastering the beam noticeably on the detector, negating our plan to use the slit to measure the spot diameter.

Now with lens voltages E1, E2, and E3 fixed, the electron gun grid (A1) and aperture (A2) voltages were varied in an attempt to minimize spot size. Once optimum settings for A1 and A2 were found, they were fixed. At this point, VE_3 was adjusted. Due to time considerations, VE_1 was left at its initial setting throughout the tests.

Once the lens voltage settings were deemed "optimum", the oscilloscope intensity control was adjusted to maximize visual contrast on the screen. Then we measured the diameter of the specular beam directly from the scope using the scope grids (1/40th of an inch) as our scale. Figure 28 shows the specular beam as viewed on the oscilloscope. These Polaroid photos were taken with exposure time of 1/25 sec. The dark areas in both photos are shadows from the shield attached to the front grounded grid ring.

At this point in the experiment, within the limitations of the oscilloscope picture, we had to make an estimate of the FWHM of the beam diameter at the detector. We determined visually that at the radius of the spot, the intensity was between 1/10th and 1/100th of the intensity of the center of the spot, with 1/20th being the specific value determined. Once this measurement was made, the beam energy was determined from an external multimeter hooked to the power control unit as described in Section III. Finally, the angle of incidence was deduced as explained in Figure 25.

Once these measurements were made, the entire procedure was repeated for a new beam energy. After all spot diameter measurements for each beam energy studied were made, we attempted to estimate the corresponding beam currents *at the sample* in the following manner. We recorded the count rate from the position computer, then converted this value to beam current *at the sample*. To do this, we took into account that the position computer "dead count" meter, whose value is the inverse of the percentage of incoming events lost (13). We also assumed that the specular beam current is .0001 the incident beam current.



Beam Energy = 80.0eV



Beam Energy = 174.0eV

Figure 28. Specular Beam as Viewed on the Oscilloscope.

Beam current measurements were made for filament currents up to the maximum recommended value of 1.9A.

Experimental Results

To determine the transfer width t via the equation

$$t = \lambda / (\text{FWHM } \Delta\theta) \cos\theta_0,$$

we need to determine the FWHM $\Delta\theta$ of the specular beam. However, we have only measured the diameter of the specular spot at the detector. The measured radius of the specular spot was estimated by *visual inspection* to have intensity between 1/10th and 1/100th of the intensity of the center of the spot, with 1/20th being the specific value determined. To get the FWHM $\Delta\theta$ and its uncertainty from this information, we first assume that the intensity distribution of our measured specular spot is Gaussian. Then we know that:

$$\alpha = \exp(-r^2 / 2 \sigma^2),$$

where α is defined as [(intensity of the spot at radius r) / (intensity of the spot at the center)], and σ is the standard deviation of the intensity distribution (1, 44). Taking the log of both sides and defining $u \equiv -\ln \alpha$, then we have the standard deviation of the spot intensity distribution σ in terms of the spot radius r and u :

$$\sigma = [r / (2u)^{1/2}].$$

Since the FWHM (Γ) of a Gaussian distribution $= 2.354\sigma$, then the FWHM of the specular spot at the detector, call it $\Gamma_{\text{specular spot}}$, is defined as:

$$\Gamma_{\text{specular spot}} = 2.354 [r / (2u)^{1/2}].$$

Now, since the distance from the sample to detector was fixed at 10.5 inches, then we have finally:

$$\text{FWHM } \Delta\theta = \{ 2.354 [r / (2u)^{1/2}] \} / 10.5 \text{ in.}$$

To calculate the uncertainty of this measurement of FWHM $\Delta\theta$, as well as the uncertainty of the corresponding measurement of the transfer width t , the standard propagation of errors method was used (1, 56). In general, for any function $x = f(p, v)$, the uncertainty in the measurement of x expressed in terms of the standard deviation σ_x is given by:

$$(\sigma_x)^2 = (\sigma_p)^2 (\partial x / \partial p)^2 + (\sigma_v)^2 (\partial x / \partial v)^2$$

where p and v have been assumed uncorrelated so that the covariance term is 0. Specific to our data, the uncertainty in the measurement of the FWHM $\Delta\theta$ is expressed in terms of the standard deviation as:

$$[(\sigma_{FWHM \Delta\theta})^2 / (FWHM \Delta\theta)^2] = [(\sigma_{\Gamma \text{ specular spot}})^2 / (\Gamma \text{ specular spot})^2] + [(\sigma_{\text{sample-detector dist}})^2 / (\text{sample-detector dist})^2],$$

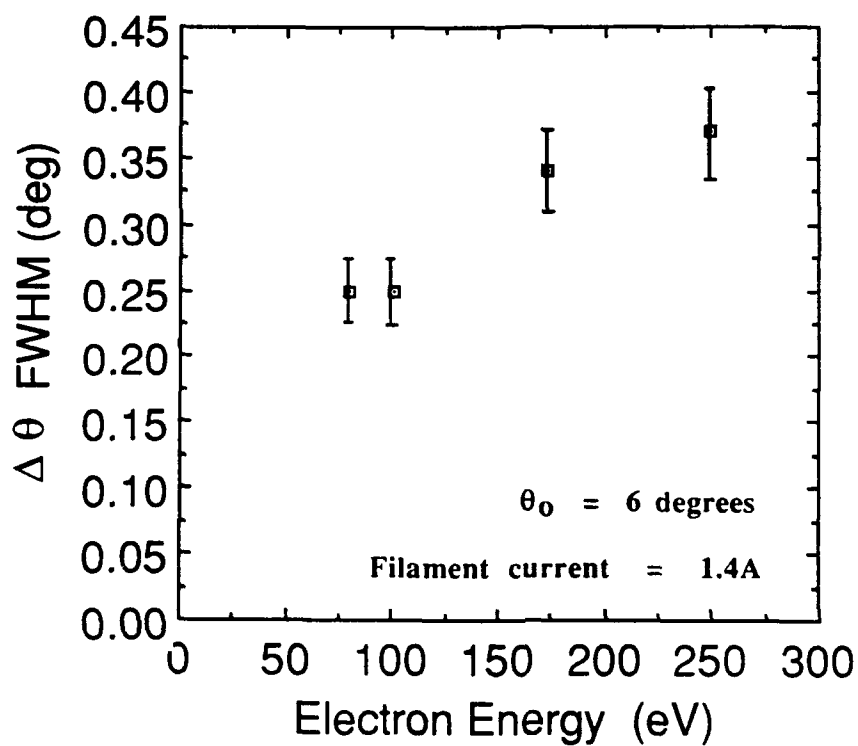
where $\sigma_{\Gamma \text{ specular spot}}$ is given by:

$$\sigma_{\Gamma \text{ specular spot}} = (2.354 / 2) [(\sigma_r)^2 \{(2u)^{-1/2}\}^2 + (\sigma_u)^2 \{-(2)^{-3/2} (r)(u)^{-3/2}\}].$$

Furthermore, the uncertainty in the measurement of the transfer width t is expressed in terms of the standard deviation as:

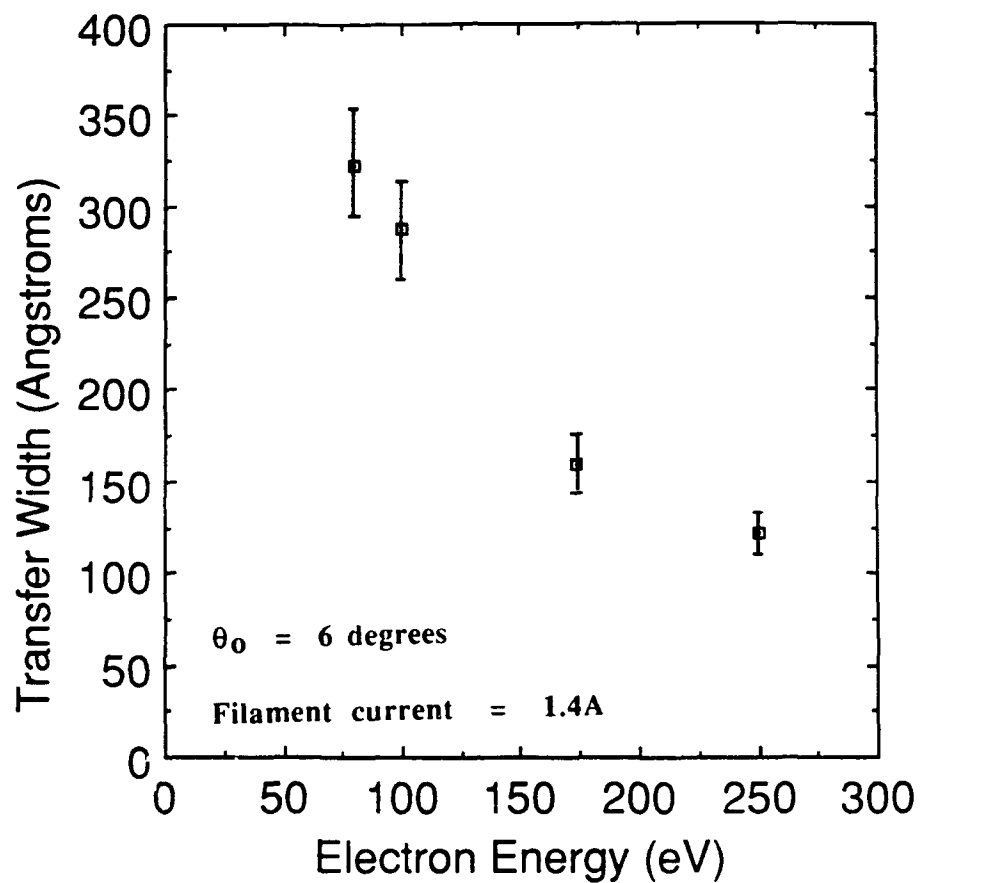
$$(\sigma_t)^2 / (t)^2 = (\sigma_\lambda)^2 / (\lambda)^2 + (\sigma_{FWHM \Delta\theta})^2 / (FWHM \Delta\theta)^2 + (\sigma_{\cos\theta_0})^2 / (\cos\theta_0)^2.$$

Figures 29 and 30 display the data and uncertainties we have found using the above methods. The graph in Figure 29 plots $FWHM \Delta\theta$ vs. the beam energy whereas that in Figure 30 plots the transfer width t vs. the beam energy. The value and uncertainty of each parameter used to calculate the $FWHM \Delta\theta$ and transfer width is listed below each graph. **Remember, this data is based on the assumption that we were able to visually determine that the intensity at the radius of the spot was between 1/10th and 1/100th of the intensity of the center.** The total height of each error bar is equal to twice the probable error P.E., or $2 \times .6745\sigma$, to indicate that the "true value"



Electron Energy (eV)	Spot Radius r	σ_r	U	σ_U	FWHM Beam spread	σ_{FWHM} Beam spread	FWHM $\Delta\theta$	σ_{FWHM} $\Delta\theta$
80.0	.050in	.012in	3.45	1.15	.045in	.0067in	.25deg	.037deg
100.5	.050in	.012in	3.45	1.15	.045in	.0048in	.25deg	.037deg
174.0	.069in	.012in	3.45	1.15	.062in	.0076in	.34deg	.042deg
250.0	.075in	.012in	3.45	1.15	.067in	.0079in	.37deg	.043deg

Figure 29. FWHM $\Delta\theta$ vs. Electron Energy.



Electron Energy (eV)	FWHM $\Delta\theta$	$\sigma_{FWHM \Delta\theta}$	$\lambda (\text{\AA})$	$\sigma_{\lambda (\text{\AA})}$	$\sigma_{\cos \theta_0}$	$t (\text{\AA})$	$\sigma_t (\text{\AA})$
80.0	.25deg	.037deg	1.37	.00171	.00091	323	49
100.5	.25deg	.037deg	1.22	.00122	.00091	288	43
174.0	.34deg	.042deg	.928	.000534	.00091	159	20
250.0	.37deg	.043deg	.775	.000310	.00091	122	14

Figure 30. Transfer Width t vs. Electron Energy for the Specular Beam.

should lie within the central value \pm P.E. with a probability of 50% (1, 115). Table 7 shows the lens voltages, filament current, and estimated beam current for each of the data points plotted in these graphs.

While we expected the FWHM $\Delta\theta$ to decrease with increasing energy, we actually observed a slight increase (0.25degrees at 80.0 eV to 0.37 degrees at 250.0 eV). This increase leads to a more severe drop-off in measured transfer width with increased energy than expected (2, 2644). We believe these findings are due to the assumption that the intensity distribution remains the same for each beam energy tested. It is evident that digital acquisition of data from the position computer is necessary to fully analyze the intensity profile of the beam.

Despite the shortcomings of the oscilloscope measurement technique, we did learn several qualitative things about the system performance. First, the focal length scaling property of this design appears valid. We found that the ratios of $V_{\text{lens}}/V_{\text{cathode}}$ which minimized the beam size at the detector remained within 2% for all lens elements except A1. A1 seemed to serve as the main focus control as was reported by Cao and Conrad (2, 2643). For our range of energies studied, the ratio $V_{A1}/V_{\text{cathode}}$ remained within 7%. We also found that for beam energies below 80 eV, spreading of the specular beam occurred for filament currents higher than 1.4 A. This spreading is presumably due to space charge effects in the beam. Finally, it was found that by applying differential steering voltage at lens A2 we achieved a more spherical spot at the detector. Referring to Table 7, we found that steering of the beam toward E2UP and E2R was

Beam Energy (eV)	Filament Current (A)	Estimated Beam Current (nA)	Grid A1 Voltage (V)	Aperture A2 Voltage (V)	Lens E1 Voltage (V)	E2 UP Voltage (V)	E2 DN Voltage (V)	E2 L Voltage (V)	E2 R Voltage (V)	Lens E3 Voltage (V)
80.0	1.40	0.32	-76.0	-52.4	112.9	25.0	23.3	23.1	24.7	27.3
100.4	1.40	0.32	-95.2	-65.9	141.7	31.1	29.1	28.8	30.9	35.9
174.0	1.40	0.32	-153.3	-114.3	245.6	54.0	50.0	49.7	53.3	61.2
250.0	1.40	0.32	-233.7	-166.8	352.8	77.5	72.4	71.5	76.7	94.4

Table 7. Electron Optics Test Parameters. This Table shows lens voltages, filament current, and estimated beam current for the beam energies sampled in this experiment. The beam current was estimated by recording the count rate from the position computer, converting this count rate to current at the detector, then converting this to current at the sample using the assumption that the specular beam current is (.0001) incident current (13, 135).

optimum. This observation indicates that slight misalignments of the lens elements about the optical axis can indeed be compensated for by E2.

V. Conclusions

The primary goal of this thesis has been to describe the design, construction, and operation of a new SPA-LEED optics system, including the required power control unit, and report the progress made to date in determining its transfer width. The design of the electron optics is a modification of the design presented by Yijian Cao and Edward H. Conrad in their article "High q-resolution electron gun for low energy electron diffraction." The features of Conrad's optics system include a "unipotential design" which allows changes in beam energy without beam defocusing. They also report high transfer widths and beam current for a wide range of beam energy. Our modifications include the incorporation of a self-contained electron gun, an electrostatic steering lens, and a new method of construction which will allow the future testing of new sources and lens systems *within the existing gun housing*. The power control unit allows control of LaB₆ emission current, control of all $V_{\text{lens}}/V_{\text{cathode}}$ ratios for beam focusing, and continuous metering of all applicable electron optics parameters.

We have tested the electron optics as part of a SPA-LEED system which incorporates a MCP/RAE position sensitive detector by studying the specular beam from a precisely cut (to within .05 degrees) Si (111) crystal. *Qualitatively*, we have learned several things about the system operation. By studying the specular beam, we have verified the "unipotential feature" of this system to the tolerances of our measurements. We have found that the steering lens does indeed reduce the effects of lens misalignment. By adjusting the differential voltage across opposite pole pieces of this lens, we can produce a more spherical spot

than without this steering of the beam. These optimum values have been noted in Table 7. Furthermore, we have found that the electron gun produces enough beam current at a cathode temperature of approximately 1650°K to approach the digital processing rate limit of the position computer (even when secondary electrons are being deflected by a retarding grid) when the detector is biased to factory specifications. More discussion of this point will follow in the **Recommendations** section.

Quantitatively, we have been able to make estimates of the transfer width and beam current from measurements made via an oscilloscope. We have determined that transfer widths over the energy range 80.0 to 250.0 eV vary from 323 to 122 angstroms, respectively. Although these values are well below those reported by Cao and Conrad, they are still a factor of 3 greater than typical commercial LEED systems. Beam currents at the sample have been found as high as 12.8 nA (with 1.9A filament current), a factor of two less than that reported by Cao and Conrad. However, testing is still in its infancy. We have been limited by the lack of a digital readout of the intensity distribution. Furthermore, due to limited testing time, we have not fully explored all combinations of lens voltages, filament currents, and optics-sample distances so as to optimize gun performance. These factors make us optimistic that with further testing and refinements, our instrumental performance will improve.

Recommendations

Before any further progress can be made in instrument performance, the position computer must be interfaced with the Macintosh IIfx computer. A

quantitative mapping of the intensity distribution on the MCP/RAE is not only necessary for eventual spot profile analysis, but it is imperative before any further refinement of the electron optics can be made. Once this interface is established, a systematic test of the electron optics must be done in which all combinations of $V_{\text{lens}}/V_{\text{cathode}}$ are explored. Furthermore, the electron optics-sample distance has not yet been varied via the track system we have designed. This degree of freedom should also be explored during testing.

Finally, we should be able to improve the transfer width of this system by placing an additional aperture on the optical axis. This will reduce the beam current, thus reducing the phase space of the beam. We have found that the maximum current at the detector was approximately 12.8 nA, registering 4×10^5 counts per second at the position sensitive detector. The maximum digital data processing rate of the position computer is 6×10^4 counts per second. Therefore, we should be able to reduce the beam current by a factor of 6 and still achieve optimum counting rates. If we assume a Gaussian beam current distribution, then we should be able to reduce the beam diameter D (see Table 2) by a factor of $(6)^{1/2}$ if we place a grounded aperture at the end of the gun housing between E3 and the sample. Since the incident electron beam diameter FWHM $T_2(\mathbf{k})$, one of the four major factors which determine the transfer width shown in Table 2, depends linearly upon D , we should then expect approximately a factor of 2 increase in transfer width. Further studies of the beam profile leaving E3 will have to be done to determine the aperture size necessary to achieve these results.

Bibliography

1. Bevington, Phillip R. Data Reduction and Error Analysis for the Physical Sciences. New York: McGraw-Hill, 1969.
2. Cao, Yijian and Edward H. Conrad. "High q-resolution Electron Gun For Low Energy Electron Diffraction." *Rev. Sci. Instrum.*, **60**, no. 8 (1989), pp. 2642-2645.
3. Gronwald, K. D. and M. H. Henzler. "Epitaxy Of Si (111) As Studied With A New High Resolving LEED System." *Surface Science*, **117** (1982), pp. 180-187.
4. Henzler, M. H. "Atomic Steps On Single Crystals: Experimental Methods And Properties." *Applied Physics*, **9** (1976), pp. 11-17.
5. Horowitz, Paul and Winfield Hill. The Art Of Electronics. 2nd ed. Cambridge: Cambridge University Press, 1989.
6. Houston, J. E. and R.L. Park. "Low-Energy Electron Diffraction From Imperfect Structures." *Rev. Sci. Instrum.*, **21** (1970), pp. 209-223.
7. Hwang, Robert Q., Ellen D. Williams, and Robert L. Park. "A High-Resolution Low-Energy Electron Diffraction Instrument." *Rev. Sci. Instrum.*, **60**, no. 9 (1989), pp. 2945-2948.
8. Klemperer, Otto. Electron Optics. 3rd ed. Cambridge: Cambridge University Press, 1971.
9. Lagally, M.G. and J.A. Martin. "Instrumentation For Low-Energy Electron Diffraction." *Rev. Sci. Instrum.* **54**, no. 10 (1983), pp. 1273-1287.

10. Lu, M. and M. G. Lagally. "The Resolving Power Of A Low-Energy Electron Diffractometer And The Analysis Of Surface Defects." *Surface Science*, **99** (1980), pp. 695-713.
11. Manufacturer's Specifications: Kimball Physics Inc.
12. Manufacturer's Specifications: Lambda Electronics.
13. Manufacturer's Specifications: Quantar Technology.
14. Manufacturer's Specifications: Valhalla Scientific.
15. McRae, E. G., R.A. Malic, and D.A. Kapilow. "A Low Energy Electron Diffraction System Using A Position-Sensitive Detector." AT&T Bell Laboratories, Unpublished.
16. Park, Robert L., J.E. Houston, and D.G. Schreiner. "The LEED Instrument Response Function." *Rev. Sci. Instrum.*, **42**, no. 1 (1971), pp. 60-65.
17. Stair, P.C. "Rapid, Pulse Counting Low-Energy Electron Diffraction." *Rev. Sci. Instrum.*, **51**, no.1 (1980), pp. 132-135.
18. Van Hove, M. A. , W. H. Weighberg, and C. M. Chan. Low-Energy Electron Diffraction. Berlin: Springer-Verlag, 1986.
18. Wang, G. C. and M. G. Lagally. "Quantitative Island Size Determination In The Chemisorbed Layer W(110) p(2x1)-0." *Surface Science*, **81**(1979), pp. 69-89.